

# **Laser-induced surface damage of optical materials: Absorption sources, initiation, growth, and mitigation**

S. Papernov\* and A. W. Schmid

Laboratory for Laser Energetics, University of Rochester, 250 East River  
Road, Rochester, NY 14623-1299, USA

## **ABSTRACT**

Susceptibility to laser damage of optical-material surfaces originates from the nature of the surface as a transitional structure between optical-material bulk and its surroundings. As such, it requires technological processing to satisfy figure and roughness requirements and is also permanently subjected to environmental exposure. Consequently, enhanced absorption caused by mechanical structural damage or incorporation and sorption of microscale absorbing defects, and even layers of organic materials, is always characteristic for optical-material surfaces. In this review physics of interaction of pulsed-laser radiation with surface imperfections for different types of optical materials (metals, semiconductors, dielectrics, etc.), mechanisms of damage initiation, damage morphology, and damage-site growth under repetitive pulse irradiation are discussed. Consideration is also given here to the surface treatments leading to the reduction of damage initiation sites, such as laser cleaning and conditioning, removal of the surface layers affected by the grinding/polishing process, and mitigation of the damage growth at already formed damage sites.

**Keywords:** Laser-induced surface damage, optical materials, continuous and localized absorption, damage growth and mitigation

## **1. INTRODUCTION**

Interaction of high-power/energy-laser radiation with optical-material surfaces is distinctly different from interaction with the material's bulk. The differences are in light absorption, intensity pattern formation, and absorbed energy dissipation. Optical material surfaces are subjected to chemo-mechanical technological processing, most frequently in some type of grinding and polishing, to meet wavefront and roughness specifications. During these processing stages, the near-surface layer undergoes structural modification caused by chemical reactions with the slurry components, incorporation and sorption of micro- or nanoscale particulates, and partial cracking and deformation frequently referred to as subsurface damage. This results in reduced mechanical strength of the material, enhanced absorption of laser radiation, and, consequently, lower laser-damage thresholds, as compared to the bulk. Another important aspect is related to the possibility of light-intensity enhancement in the surface proximity due to constructive interference between incident and reflected waves. Finally, absorbed-energy-dissipation processes are affected by the nearby free surface. In the case of localized absorption of pulsed laser energy, a compressive shock wave released from an absorption center upon reflection from the free surface converts into a rarefaction (tensile) wave. Since tensile material strength is usually much lower than compressive strength, it might lead to early material failure. Also, considering energy dissipation through heat conduction, the free surface effectively renders an adiabatic boundary, which causes the temperature buildup to facilitate the damage process. These considerations clearly show that surfaces of most optical materials for high-power-laser applications are more susceptible to damage than bulk, and this review paper is intended to summarize the most important findings related to surface damage of optical materials. The challenge here lies in the enormous amount of scientific material generated during this time period, the huge variation in laser-radiation parameters used (wavelength, pulse width, repetition rate, spot size, etc.), and optical materials studied. To make this paper reasonable in

size and representative in content, the authors decided to place an emphasis on surface damage initiated by *nanosecond-scale pulsed-laser* radiation widely used in fusion-scale lasers, lithography, etc. Similarly, in an attempt to narrow the scope of the materials considered, in the case of transparent dielectrics we focused on most-studied materials like *fused silica*, which is reflected in many topics of this paper.

First, we consider mechanisms of surface damage initiated by continuous (nonlocalized) absorption in metals and semiconductors. Attention is given here to surface-damage mechanisms reflected in damage morphology, laser-spot-size dependence, and the comparison of single- and multiple-pulse damage. Surface damage in transparent dielectrics driven by absorption in localized defects (inclusions) makes up the majority of this paper, with a focus on the sources of localized absorption, physics of localized absorber-driven damage, and the use of model glass systems with artificial absorbers for damage-mechanism clarification. Consideration is also given to damage morphology, structural modifications in damaged material, and damage growth under repetitive pulsed irradiation. We also discuss the relation between entrance and exit surface damage, as well as damage initiated by adsorbed metallic particulates. The conclusion is devoted to the improvement of surface-damage resistance through laser conditioning and advanced surface processing leading to minimization of near-surface absorption. Finally, technological achievements in surface-damage mitigation are presented and discussed.

## 2. SURFACE DAMAGE INITIATED BY CONTINUOUS (NONLOCAL) ABSORPTION IN METALS AND SEMICONDUCTORS

### 2.1 Mechanisms of surface damage in metals and semiconductors

Relatively low reflectivity of metals<sup>1</sup> and strong absorption of semiconductors in the ultraviolet (UV) and visible spectral range<sup>2</sup> limits the application of these materials in high-power-laser systems (mostly as mirrors) to the infrared (IR) portion of the spectrum (see Figs. 1 and 2). Even in the IR spectral range, the reflectivity of the best metals, i.e., Ag, Au, and Cu, does not exceed 99.5%, leaving ~1% for absorption—a fairly significant value considering the power densities to be dissipated are of the order of ~kW/cm<sup>2</sup> for continuous wave (cw) irradiation. In the case of pulsed irradiation, different types of damage morphology corresponding to different levels of laser fluence are observed.<sup>3</sup> As shown schematically in Fig. 3, for a diamond-turned Cu mirror irradiated by 10-ns, 1064-nm wavelength pulses with laser fluences increasing from 8.8 J/cm<sup>2</sup> to 12.7 J/cm<sup>2</sup>, slip, or plastic deformation, is initially observed, then a ripple pattern formation, followed by flat melting, and finally, boiling morphologies is seen. Slip, or plastic deformation, in a form of very fine roughening<sup>4</sup> [see Fig. 4(a)], caused by stresses exceeding the yield stress of the material generated in response to local heating of the metallic surface,<sup>5</sup> is illustrated in Fig. 4(b). Ripple pattern is a universal damage morphology observed in metals, semiconductors, and transparent dielectrics.<sup>6-9</sup> Ripple origin is attributed<sup>10</sup> to interference between incident and surface waves scattered on subwavelength imperfections (corrugations, etc.). Such a

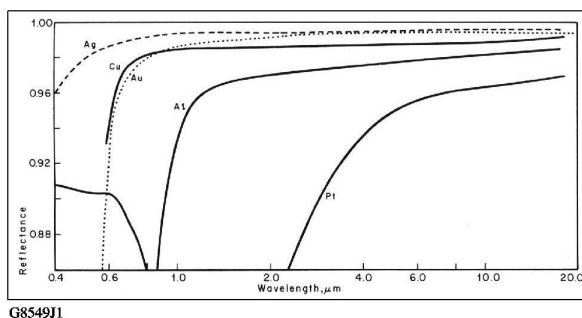


Fig. 1. Visible and infrared reflectance of certain metals.<sup>1</sup>

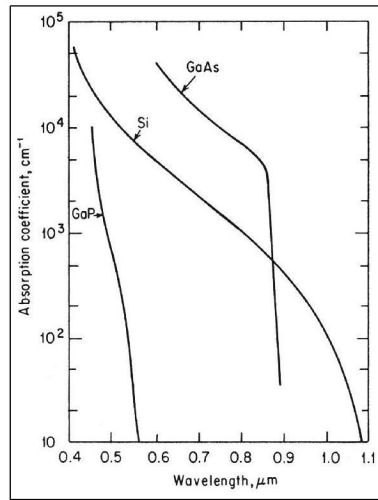


Fig. 2. Absorption of various semiconductors at 300 K (Ref. 2).

G8549J2

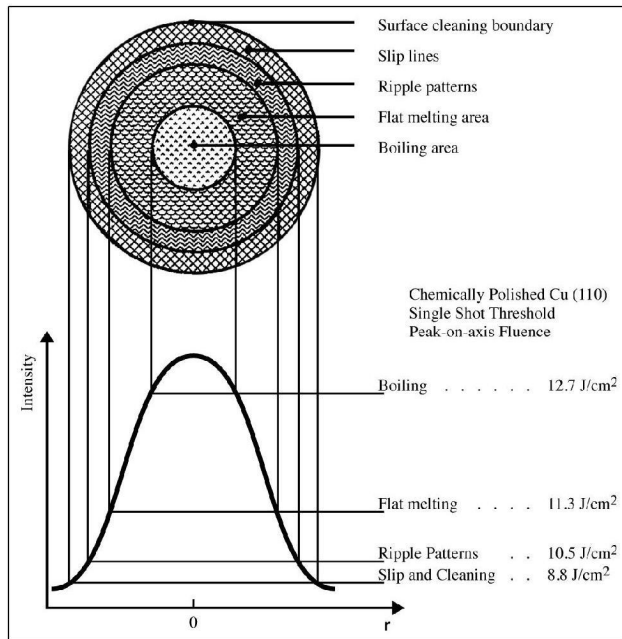
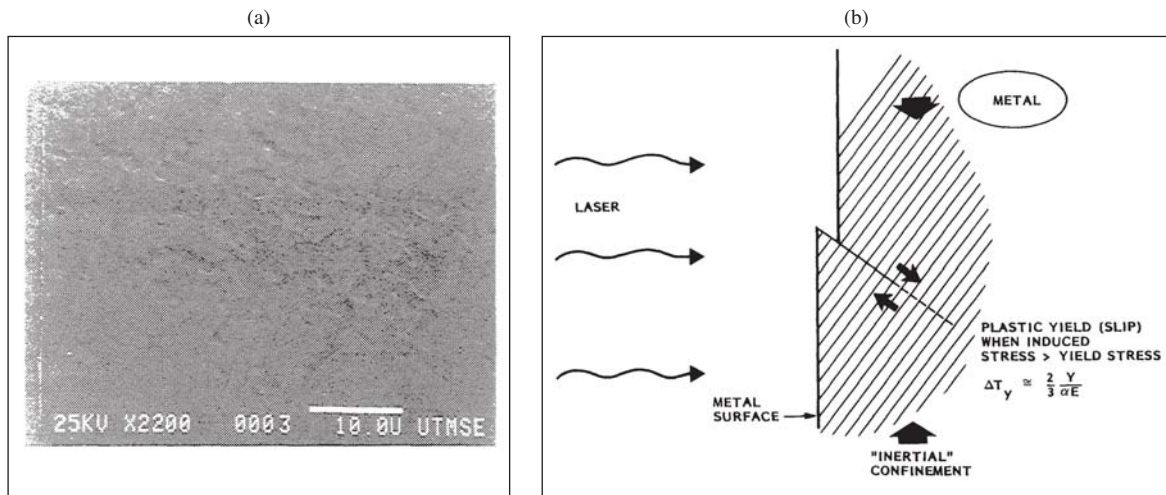


Fig. 3. Schematic presentation of diamond-turned Cu surface-damage-morphology evolution with laser fluence (after Jee *et al.*<sup>3</sup>).

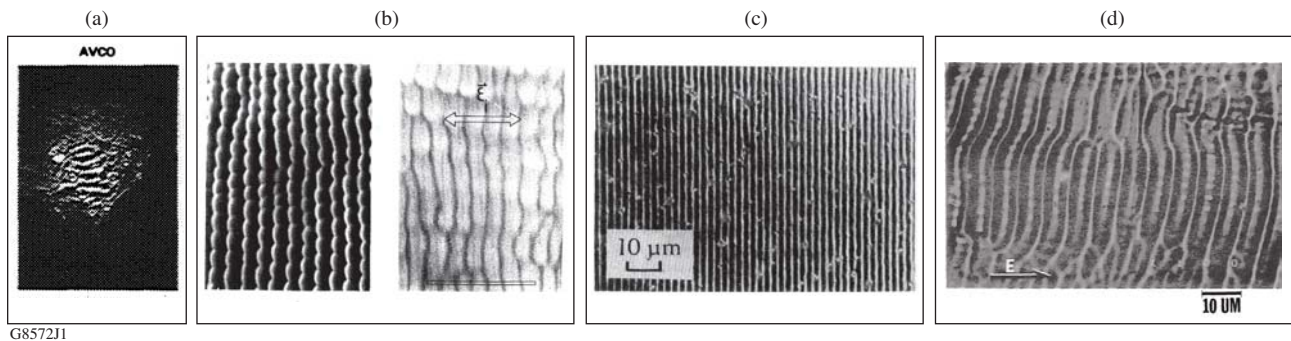
G8570J1

mechanism is supported by measured fringe spacing  $d \approx \lambda/(1 \pm \sin \theta)$ , where  $\lambda$  is the wavelength,  $\theta$  is the incidence angle, fringe orientation normal to electric vector of the incident wave, and was observed for cw, pulsed-laser radiation, and a wavelength ranging from UV to IR (see Fig. 5). Flat-melting onset fluence is usually slightly above ripple-formation onset, and melting morphology clearly shows the features of molten material flow [see Fig. 6(a)]. Figure 6(b) depicts the frequent case of melting initiated at surface-defect sites characterized by enhanced absorption.



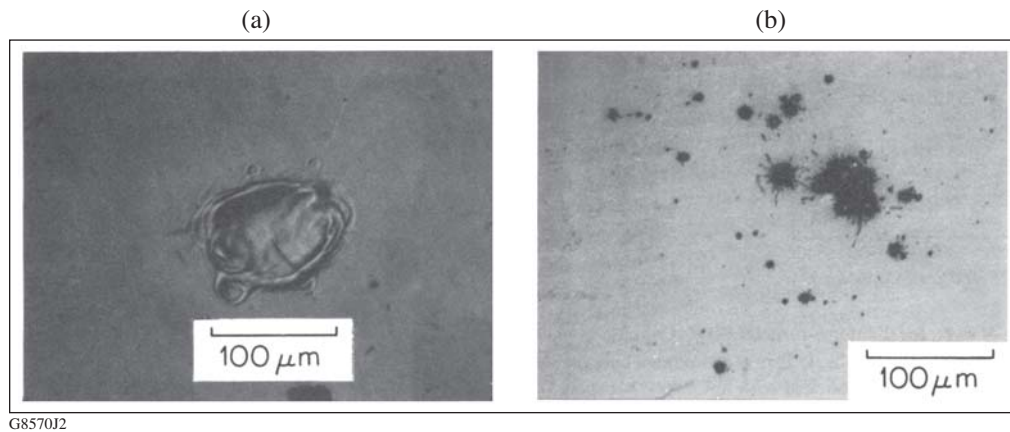
G8571J1

Fig. 4. Plastic deformation (slip) (a) on the Cu surface induced by 1064-nm, 20-ns pulses ( $N = 3000$ ) with an average fluence of  $3.28 \text{ J/cm}^2$  (after Jee *et al.*<sup>4</sup>); (b) schematic presentation of slip (after Musal<sup>5</sup>).



G8572J1

Fig. 5. Ripple patterns on (a) diamond-turned Cu mirror,  $\lambda = 10.6 \mu\text{m}$ ,  $t = 100 \text{ ns}$  (after Porteus *et al.*<sup>6</sup>), (b) Cd film on  $\text{SiO}_2$  substrate,  $\lambda = 257 \text{ nm}$ , cw (after Brueck *et al.*<sup>7</sup>), (c) polished Ge,  $\lambda = 1.06 \mu\text{m}$ ,  $t = 20 \text{ ns}$  (after Young *et al.*<sup>8</sup>), (d) KCl,  $\lambda = 10.6 \mu\text{m}$ ,  $t = 100 \text{ ns}$  (after Mansour *et al.*<sup>9</sup>).



G8570J2

Fig. 6. Flat melting morphology on diamond-turned Cu irradiated at (a)  $10.6 \mu\text{m}$ , beam-spot size  $w = 110 \mu\text{m}$  and (b)  $1.06 \mu\text{m}$ ,  $w = 250 \mu\text{m}$  (after Lee *et al.*<sup>11</sup>).

## 2.2 Multiple-pulse-irradiation effects and laser-spot-size dependence

Typical damage-threshold behavior for multiple-pulse irradiation of metallic surfaces with small, submillimeter, beam-spot size is characterized by threshold reduction with an increasing number of pulses. Considering plastic deformation (slip) as a main damage mechanism, such threshold behavior can be explained by an accumulation of plastic deformation caused by consecutive pulse irradiation. For example, Fig. 7 shows that the cumulative effect from multiple-pulse irradiation (1064 nm, 22 ns,  $N = 10^4$ ) of the Cu surface can lead to an  $\sim 3$ -fold reduction in the threshold for a small 50- $\mu\text{m}$  spot size. The same graph points to different threshold behavior with a spot size for single and multiple pulses. In this particular case, single-pulse threshold is controlled by defects and threshold reduction with a spot size related to an increasing probability of finding an absorbing defect within the beam spot. Contrary to that, the multiple-pulse ( $N = 10^4$ ) threshold is defined by stress, where amplitude depends on temperature gradient. By using linear-thermoelastic theory, the power density producing stress equal to the yield strength may be expressed for the Gaussian spot size  $w$  as follows:<sup>11</sup>

$$I(w) \approx (2\pi e)^{1/2} (1-\nu) \rho C \sigma w / 4AE\alpha\tau, \quad (1)$$

where  $\nu$ ,  $\rho$ ,  $C$ ,  $A$ ,  $E$ ,  $\alpha$ ,  $\sigma$ , and  $\tau$  are Poisson's ratio, material density, specific heat, optical absorbance, Young's modulus, thermal-expansion coefficient, surface-yield strength, and pulse width, respectively. One can see from the formula above that the threshold grows roughly linearly with spot size  $w$ , which reflects a reduction in temperature gradient and stress.

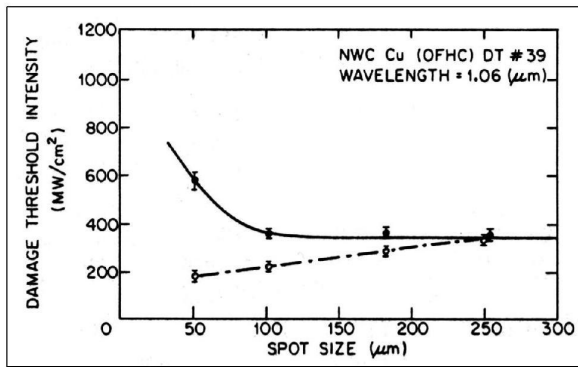


Fig. 7. Threshold spot-size dependence for single- (solid circles) and multiple-pulse (open circles,  $N = 10^3$ ) 1.06- $\mu\text{m}$ , 22-ns irradiation of Cu surface (after Lee *et al.*<sup>11</sup>).

In the case of cw irradiation of metal mirrors it was demonstrated<sup>12</sup> that catastrophic damage is strongly linked to reaching the critical temperature, in most cases the melting point, by the mirror material. It was also shown using thermal calculations that the beam-spot-size  $R$  to mirror- (substrate) thickness  $L$  ratio has a strong impact on mirror performance. The threshold condition is then best characterized by the ratio  $P/R$ , where  $P$  is the threshold power, not by power density, as in the case of pulsed irradiation. Consequently, the scaling law linking small (test), millimeter-scale-beam catastrophic damage threshold to large-beam threshold conditions takes the following form:

$$P/R^2 = P_t/R_t \times S/L, \quad (2)$$

where index  $t$  denotes test beam parameters and  $S$  is the beam-shape factor equal to unity for the uniform case and close to unity for the Gaussian case.

## 2.3 Ultrashort-pulse laser interaction with metal surfaces

Interaction of ultrashort, femtosecond laser pulses with absorbing materials is distinctively different than, for example, the case of nanosecond pulses. During ultrashort-pulse irradiation, energy is deposited exclusively in a free-electron

subsystem, and coupling to phonons (conversion to heat) takes place after a laser pulse with a characteristic time constant of 1 to 10 ps (Ref. 13). The result is very localized heating, melting, and ejection of the material upon reaching ablation threshold that allows for submicrometer precise micromachining of the materials with focused femtosecond laser pulses. For example, Fig. 8 shows the Laser Zentrum Hannover logo engraved in copper using 150-fs pulses.<sup>14</sup>

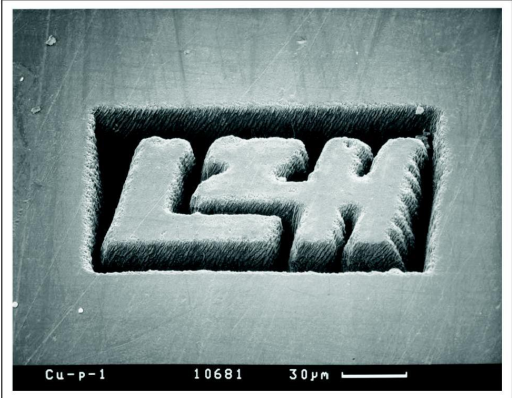


Fig. 8. Laser Zentrum Hannover logo on the polished Cu surface produced with 780-nm, 150-fs pulses,  $N = 10^4$  (after Nolte *et al.*<sup>14</sup>).

### 3. SURFACE DAMAGE INITIATED BY LOCALIZED ABSORPTION IN TRANSPARENT DIELECTRICS

#### 3.1 Sources of localized absorption in dielectric material near the surface layer

As previously outlined in Sec.1, optical-material-surface processing inevitably modifies the near-surface layer. In the case of glass materials, schematically presented in Fig. 9, the very top (~100 nm) chemically modified layer is followed by a subsurface damaged structure comprised from cracks extending up to 100  $\mu\text{m}$  in depth after the grinding stage.<sup>15</sup> These cracks may contain trapped abrasive particulates and other contaminants providing for absorption on laser irradiation. A recently developed, additional multistep-surface process that removes subsurface damage and thus minimizes near-surface absorption is discussed in Sec. 4. In the case of optical glass, other sources of localized absorption, although in very low densities for laser quality materials, might be defects that are not surface specific. These are micro- and nanoscale stones from the starting material, or metal particulates from the crucible, generated during the glass-melting process in glass volume and, statistically, may also be found in the near-surface layer.

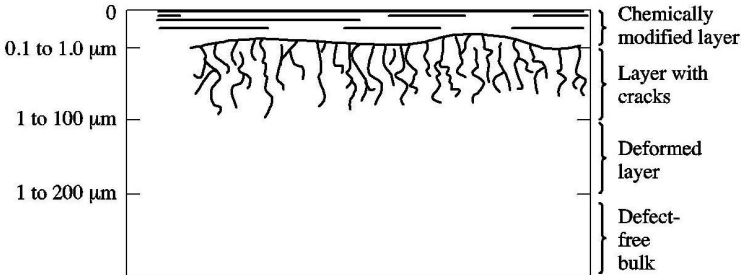


Fig. 9. Schematic of the subsurface damage.

### 3.2 Thermal approach to localized absorber-driven damage

The classical approach to localized absorber-driven damage is based on the definition of damage threshold as reaching critical temperature  $T_c$  by the absorber-surrounding matrix. A one-dimensional thermal-diffusion model, considering heat conduction as the dominating energy-dissipation mechanism from the laser-heated absorber, was first explored in the context of laser damage by Hopper and Uhlmann<sup>16</sup> and further developed by other authors.<sup>17-19</sup> We will follow here the approximation of Feit and Rubenchik,<sup>19</sup> assuming (1) that absorber thermal conductivity is much higher than the conductivity of the matrix and (2) that the temperature is homogeneous inside the absorber. The temperature of the matrix surrounding the absorbing particle can be found from the heat equation

$$\partial T / \partial t = D \nabla^2 T \quad (3)$$

with boundary conditions at  $r = a$  (particle radius)

$$\alpha I(t) = -4k(\partial T / \partial r)_{r=a} + 4/3 \rho C a (\partial T / \partial r)_{r=a}, \quad (4)$$

where  $\alpha$ ,  $\rho$ , and  $C$  are absorptivity ( $\alpha = \sigma \pi a^2$  and  $\sigma$  is the absorption cross-section), mass density, and heat capacity of the particle, respectively;  $D$  and  $k$  are thermal diffusivity and thermal conductivity of the matrix, respectively; and  $I$  is laser intensity.

For the rectangular heating pulse of duration  $\tau$ , the solution of Eq. (3) is

$$T = T_0 \left[ 1 - \exp\left(-4D\tau/a^2\right) \right], \quad (5)$$

where  $T_0 = \alpha F a / 4k\tau$ ,  $D = 3k/4\rho C$ , and  $F$  is laser fluence.

The temperature reaches a maximum value for absorber size (see Fig. 10) comparable with the thermal diffusion length

$$2a = 3.6\sqrt{D\tau}. \quad (6)$$

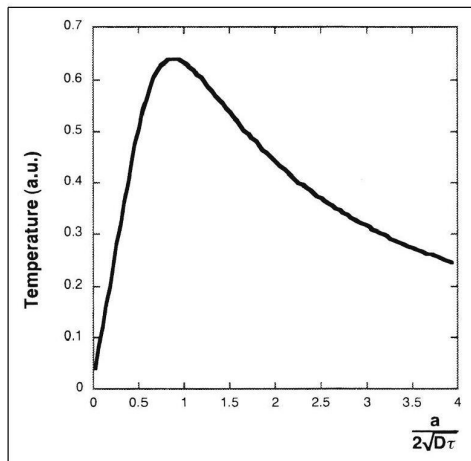


Fig. 10. Absorber temperature as a function of normalized absorber radius (after Feit and Rubenchik<sup>19</sup>).

G8555J1

Assuming  $T = T_c$ , the threshold fluence from Eq. (5) is

$$F_{th} = 6.3 T_c k \sqrt{\tau/\alpha} \sqrt{D}. \quad (7)$$

Formula (7) highlights the widely used pulse-length scaling

$$F_{th} \sim \sqrt{\tau}. \quad (8)$$

In the case when particle absorptivity is a function of size  $a$ , pulse-length scaling will not follow Eq. (8). For example, Fig. 11 presents results<sup>20</sup> of exact  $F_{th} = F_{th}(\tau, a, \lambda)$  dependence calculations for an Al absorber embedded in a  $\text{SiO}_2$  matrix. One can notice strong threshold pulse-width dependence ( $\sim \tau^{0.87}$ ) for small ( $\sim 10$ -nm) absorbers explained by volume absorption and by the kinetics of heat dissipation. For large,  $1\text{-}\mu\text{m}$  particles, absorption takes place in a skin-depth layer that is small compared to the particle radius and is accompanied by heat diffusion inside the particle. This process is much faster than heat diffusion into the matrix and strongly affects temperature kinetics and spatial profile, leading to much slower  $\sim \tau^{0.3}$  threshold pulse-width scaling. One can also see that thresholds for small particles are much lower for 351 nm, compared to 1053 nm (due to higher Mie<sup>21</sup> absorption cross-sections at 351 nm) and show no wavelength dependence for particles larger than  $1\ \mu\text{m}$ .

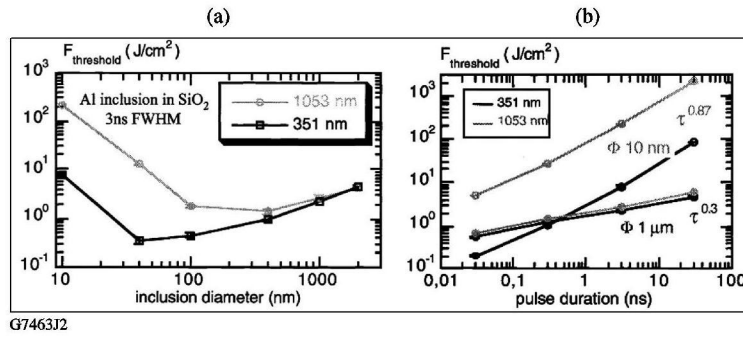


Fig. 11. 351-nm and 1053-nm damage thresholds as a function of (a) Al-particle size; (b) pulse duration for 10-nm and 1000-nm Al-particle sizes (after Bonneau *et al.*<sup>20</sup>).

### 3.3 Probabilistic nature of damage driven by localized absorbers

Damage initiated by localized absorbers under typical damage-test conditions utilizing millimeter-scale laser-beam spots is highly probabilistic by nature. The result (damage or no damage) is linked to the probability of finding an absorber within a portion of the beam spot where fluence exceeds the threshold for absorber failure. The following description was first suggested by Foltyn<sup>22</sup> and later developed by other authors.<sup>23–25</sup> In the case of illumination with Gaussian spatial-energy distribution

$$F(r) = F_0 \exp\left[-2(r/L)^2\right], \quad (9)$$

where  $F_0$  is the maximum fluence ( $F_0 > T$ , threshold) and  $L$  is the beam radius at the  $e^{-2}$  level; damage probability  $P$  takes the following form:<sup>25</sup>

$$P(F_0) = 1 - (F_0/T)^{-(d \times S/2)}, \quad (10)$$

where  $S = \pi L^2$  and  $d$  is the absorber surface density. In Fig. 12, a damage-probability modeling example is presented for a sample containing three different types of absorbers. The presence of an additional type of absorber is manifested by a

change in the slope of the curve. The best fit of experimental  $P$  curves provides data on threshold fluence and absorber density<sup>26</sup> (see Fig. 13).

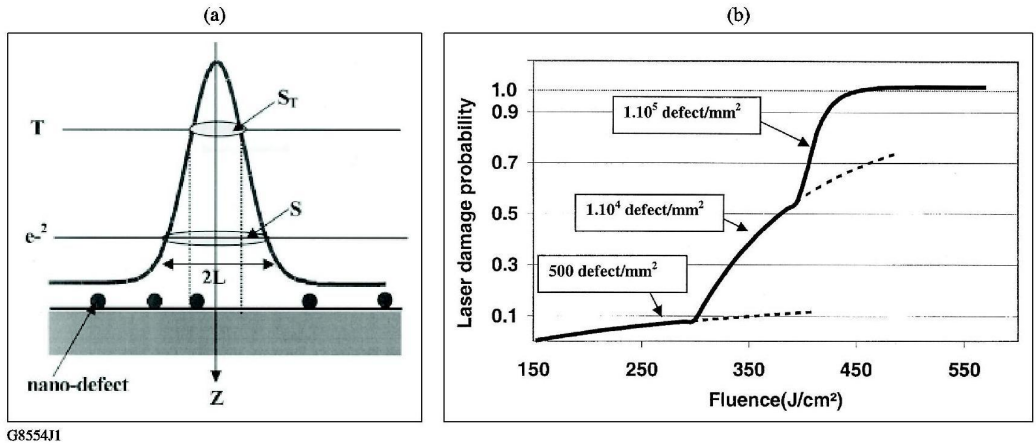


Fig. 12. Damage-probability modeling: (a) illustration of the probability of the presence of absorbing defects in the region  $S_T$ , where energy density is greater than threshold  $T$ ; (b) Damage probability curve for three kinds of defects:  $d_1 = 500 \text{ mm}^{-2}$ ,  $T_1 = 150 \text{ J/cm}^2$ ;  $d_2 = 10^4 \text{ mm}^{-2}$ ,  $T_2 = 300 \text{ J/cm}^2$ ;  $d_3 = 10^5 \text{ mm}^{-2}$ ,  $T_3 = 400 \text{ J/cm}^2$  (after Natoli *et al.*<sup>25</sup>).

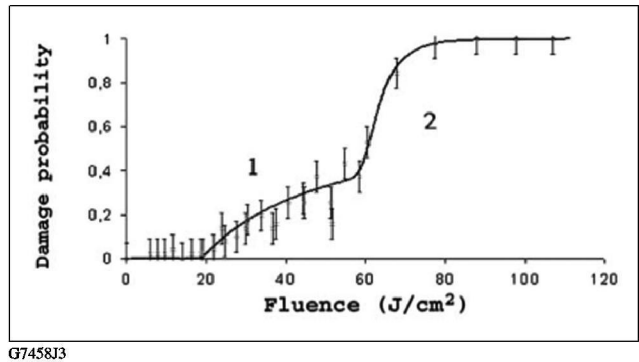


Fig. 13. Experimental damage-probability data and theoretical best-fit (solid line) for a  $\text{Ta}_2\text{O}_5$  coating irradiated by 1064-nm, 5-ns pulses. Two kinds of defects are identified:  $d_1 = 1.6 \times 10^4 \text{ mm}^{-3}$ ,  $T_1 = 19 \text{ J/cm}^2$ , and  $d_2 = 5 \times 10^5 \text{ mm}^{-3}$ ,  $T_2 = 60 \text{ J/cm}^2$  (after Krol *et al.*<sup>26</sup>).

### 3.4 Modeling surface-damage morphology using brittle-fracture models

The main features of surface-damage morphology are craters: detailed studies of crater symmetry, aspect ratio, and wall microstructure provide insight into the mechanisms of damage initiation and growth. Theoretical studies of crater formation using numerical modeling are very limited due to the lack of information on temperature dependencies of optical, thermal, and mechanical parameters of the materials at high temperatures, up to  $10^4 \text{ K}$ , characteristic of the damage process. Fracture propagation initiated by pulse laser heating of near-surface particles is one of the crater-formation scenarios. Numerical finite-element calculations using brittle-fracture models can predict the kinetics of propagation and final shape of the crack. Figure 14 depicts the results of calculations, using the *DYNA* 2-D code,<sup>27</sup> of crack propagation in fused silica caused by 355-nm, 3-ns, 10-J/cm<sup>2</sup> laser heating of a 100-nm cerium particle located 300 nm beneath the surface. The model takes into account mechanical parameter dependence on loading time and energy density and predicts a cone-shaped crater [see Fig. 14(c)] after crashed material removal. Another example is numerical

modeling of crack-propagation kinetics around a 1- $\mu\text{m}$  Al inclusion embedded near a fused-silica surface and subjected to heating by a 351-nm, 3-ns square pulse (see Fig. 15). In this case the *DELPOR*<sup>28</sup> 1-D hydrodynamic code capable of computing laser-energy deposition (including E-field distribution) was used as the preprocessor for *HESIONE*,<sup>28</sup> a 2-D finite-element hydrodynamic code predicting fracture evolution under tensile and compressive stresses. The *DELPOR* code takes into account thermal conduction, radiative transfer and ionization by UV light, propagation of shock waves, and all solid-to-plasma phase transitions, although in this case, no absorption was considered in the inclusion-surrounding matrix. This simulation shows that crack propagation for the chosen irradiation parameters has speed of the order of  $\sim 1$  km/s, comparable to the speed of sound.

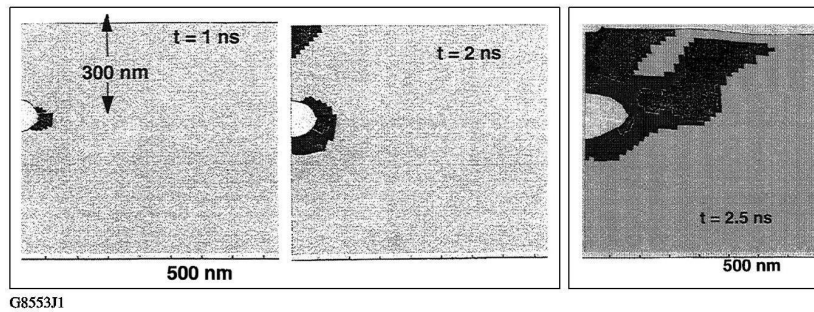


Fig. 14. Fracture growth in fused silica initiated by absorption inside a 100-nm cerium particle irradiated by a 355-nm, 3-ns pulse with a fluence of  $10 \text{ J/cm}^2$  (a) after 1 ns of irradiation; (b) 2 ns, and (c) 2.5 ns (after Feit *et al.*<sup>27</sup>).

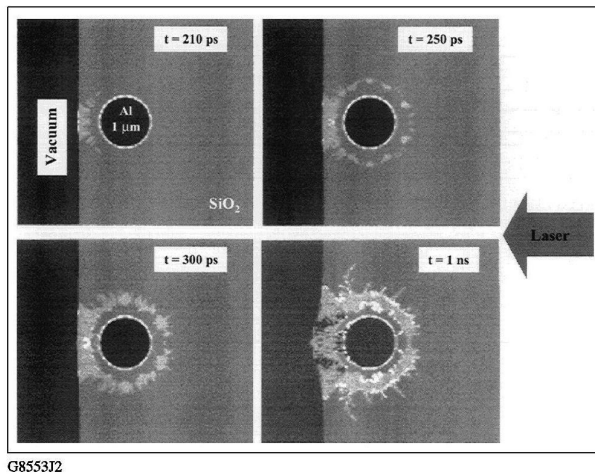


Fig. 15. Crack propagation around 1- $\mu\text{m}$  Al inclusion embedded in fused silica and irradiated by a 351-nm, 3-ns square pulse with a fluence of  $20 \text{ J/cm}^2$  (after Bonneau *et al.*<sup>28</sup>).

### 3.5 Phenomenological theory of crater formation based on the thermal explosion mechanism

Complex computations involved in numeric modeling of crater formation can be avoided in the phenomenological approach,<sup>29</sup> linking crater size to the total energy absorbed from laser pulse; in particular, the volume beneath the surface. Both total energy and volume can be estimated using the thermal-explosion theory.<sup>30</sup> According to this theory, reaching critical temperature in the vicinity of the absorbing defect leads to the effective conversion of the defect-surrounding matrix into the absorbing medium, rapid heating, and ionization (thermal explosion). The result is a plasma “fire-ball” formation (see Fig. 16), with energy density well above the evaporation energy. The plasma-ball radius  $a$  grows exponentially with laser fluence  $F$

$$a = a_0 \exp \gamma, \quad \gamma \sim F. \quad (11)$$

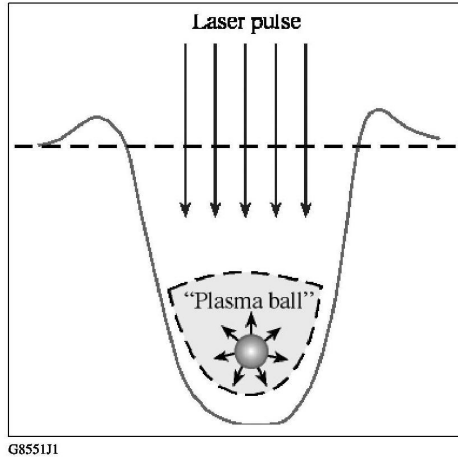


Fig. 16. Schematic of the plasma-ball formation around an absorbing defect.<sup>31</sup>

At high laser fluences, growth of the plasma ball saturates with the diameter, reaching a maximum value of the order of  $\lambda$ . In this case absorbed energy can be estimated as

$$E = F\pi\lambda^2. \quad (12)$$

Part (~10%) of the released energy  $E$  is converted into the hydrodynamic motion of the highly heated and crashed material (which can be treated as incompressible liquid) leading to crater formation. Crater radius  $R$  as a function of the absorber depth  $h$  is given by the expression<sup>29</sup>

$$R^2 = h^{2/3} \left( h_d^{4/3} - h^{4/3} \right), \quad (13)$$

where  $h_d$  is a maximal burial depth for which a crater is formed,  $h_d \sim E^{1/4}$ . For an explosion with fixed energy  $E$ , there is a depth  $h_m$  for which the crater has maximum size  $R_m$  (see Fig. 17):

$$R_m = \sqrt{2h_m} \approx 0.6 h_d, \quad h_m \approx 0.44 h_d. \quad (14)$$

This theory provides tools for simple crater-size estimates at high laser fluences. Nevertheless, for obvious reasons, it cannot be used for damage-threshold evaluation.

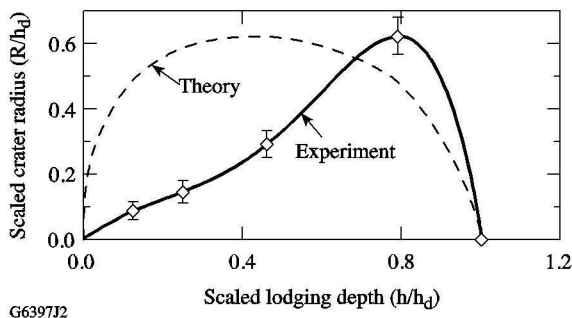


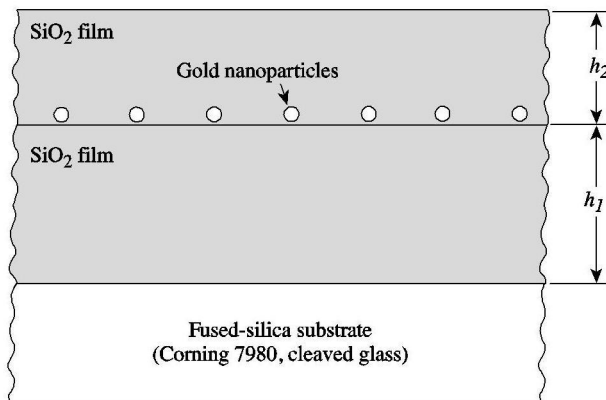
Fig. 17. Scaled crater radius versus scaled particle-lodging depth. Experimental data are taken<sup>31</sup> at a 351-nm, 0.5-ns fluence of 1.7 J/cm<sup>2</sup>, corresponding to the crater formation threshold for a 18.5-nm-particle lodging depth of 240 nm ( $h_d = 240$  nm).

### 3.6 Using model glass systems with artificial calibrated absorbers for surface-damage mechanism clarification

Experimental validation of any theory of localized absorber-driven damage is impossible without a comprehensive knowledge of defect geometry and, at least, optical and thermal parameters. Unfortunately, characterization of localized

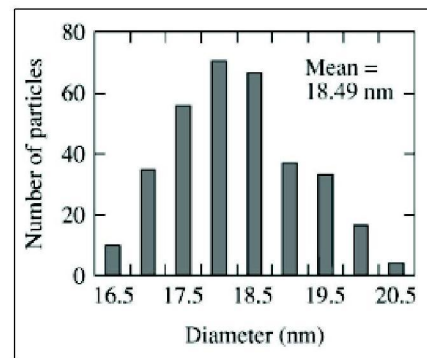
absorbing defects in laser-quality dielectric materials is a real challenge due to low densities and small, usually submicrometer, sizes. This situation makes it practically impossible for a meaningful comparison of experimental results with theoretical modeling and stimulated implementation of model thin-film-based glass systems with well-characterized, artificial nanoscale absorbers. Typically, such a model system would consist of gold nanoparticles embedded inside a silica film deposited on a fused-silica-glass substrate, as shown in Fig. 18. Well-known optical and thermal characteristics, narrow-size distributions (Fig. 19), chemical stability, and availability in the form of gold colloids or powders make gold nanoparticles the preferable choice for artificial absorbing defects. Silica-film material is known for high-damage resistance in high-power-laser applications. This makes it possible to study gold-particle-driven damage without interference from damage driven by intrinsic silica-film defects. The majority of studies with model systems were carried out using UV, nanosecond-pulsed irradiation (351/355 nm, 0.5 to 8 ns) that proved to be very effective in damage initiation through interaction with nanoscale absorbers.<sup>32,33</sup> Experiments with artificial gold absorbers, ranging in size from 2 to 600 nm, produced several important results related to different stages of the surface-damage process:

1. Even a few-nanometer-sized gold particles embedded at a 60-nm depth can significantly ( $\sim 3\times$  for 1.9-nm-average-diam particles, see Fig. 20) reduce the intrinsic silica-damage threshold.<sup>34</sup>
2. Irradiation at subthreshold fluences may cause dispersion of the absorbers and diffusion of the gold into the surrounding matrix as indicated by photothermal microscopy.<sup>35</sup> This result provides insight into the possible mechanism of UV laser conditioning of glass materials.
3. Comparison of energy absorbed by gold particles  $E_{\text{abs}}$  (Mie theory) and energy required for crater formation  $E_{\text{cr}}$  [atomic force microscopy (AFM) analysis] gave an unambiguous result:<sup>34</sup>  $E_{\text{abs}} \gg E_{\text{cr}}$ , which implies that absorption takes place in larger than particle volume (absorption delocalization). This result provides direct evidence for plasma-ball formation and proves the validity of the thermal explosion mechanism described in Sec. 2.5.



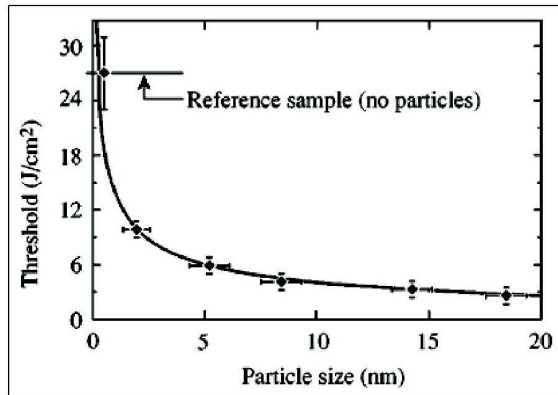
G8550J1

Fig. 18. Schematic presentation of the SiO<sub>2</sub> sample with embedded gold nanoparticles.



G8550J2

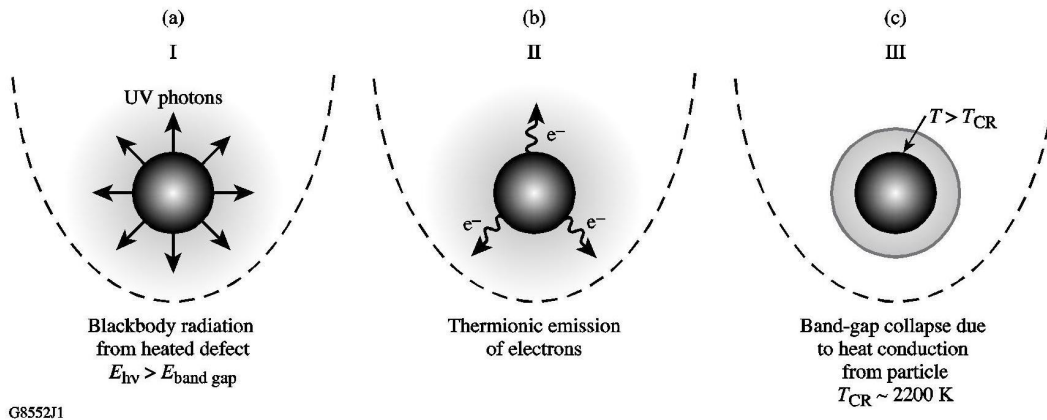
Fig. 19. 18.5-nm average diameter colloidal-nanoparticle-size distribution, provided by the supplier<sup>31</sup> (Ted Pella, Inc.).



G8550J3

Fig. 20. 351-nm, 0.5-ns silica-damage thresholds as a function of embedded gold nanoparticle size.<sup>34</sup>

Three possible mechanisms converting the absorber-surrounding matrix into an absorbing medium are identified (see Fig. 21). First, photoionization by photons with energy exceeding the 8.9-eV silica band gap and originating as the UV part of the black-body radiation from absorber heated to several thousand degrees;<sup>30</sup> second, through thermionic emission of electrons from a heated metallic absorber;<sup>36</sup> and third, due to matrix band-gap collapse upon reaching critical temperature at the absorber/matrix interface and followed by direct laser ionization. Feasibility of the last process was recently demonstrated<sup>37</sup> by heating silica glass with a CO<sub>2</sub> laser and simultaneous irradiation with 355-nm pulses. A dramatic drop (order of magnitude) in 355-nm damage threshold upon the silica surface reaching a temperature of ~2200 K provided clear evidence of the band-gap collapse.

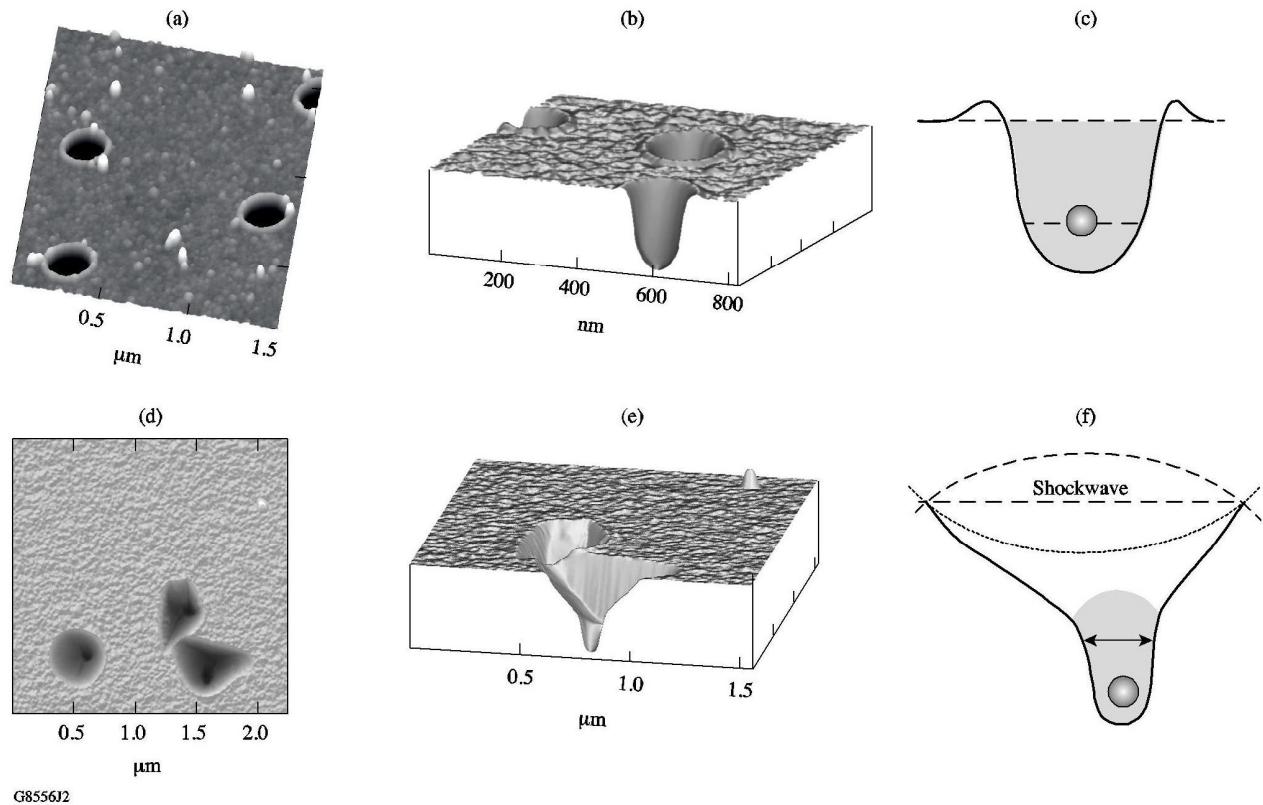


G8552J1

Fig. 21. Schematic presentation of three mechanisms transforming absorber-surrounding matrix into absorbing medium: (a) photoionization by UV radiation from heated absorber; (b) thermionic emission of electrons; and (c) heat-transfer-induced band-gap collapse.

### 3.7 Glass damage morphology and its link to the mechanism of crater formation

Two types of damage-crater morphology were found in model systems with gold absorbers.<sup>31</sup> One, shown as a regular crater in Figs. 22(a–c), is typical for melting and evaporation and has circular lateral symmetry, single-cone shape, smooth walls, and an elevated rim pointing to melted material flow and resolidification. Regular craters are usually formed for relatively shallow absorber locations, such that the melt front accompanying the plasma-ball front reaches the material surface [see Fig. 22(c)]. The second crater morphology (complex crater) is usually observed when the absorber



G8556J2

Fig. 22. Characteristic crater morphologies produced by 351-nm, 0.5-ns irradiation of 18.5-nm particles lodged at different depths: (a) regular crater, surface plot, 60-nm absorber lodging depth;<sup>31</sup> (b) cross-sectional view of regular crater;<sup>38</sup> (c) schematic presentation of the melt front inside regular crater; (d) complex crater, surface plot, 190-nm-absorber lodging depth;<sup>38</sup> (e) cross-sectional view of complex crater;<sup>38</sup> (f) schematic presentation of the melt front and shock wave inside complex crater.

lodging depth exceeds some critical value.<sup>31</sup> These craters<sup>31,38</sup> [see Figs. 22(d–f)] exhibit a double-cone cross-sectional profile, random lateral shape with sharp corners, and the absence of an elevated rim, all indicating that the upper portion of the crater is removed by fracture. On the other hand, smooth crater walls point to reaching the melting temperature inside the crater. The crater-formation scenario for such a complex crater may include plasma-ball formation within the bottom cone (where the seeding gold absorber is located) accompanied by a strong shock wave launched toward the surface [see Fig. 22(f)]. Upon reflection from the surface, a tensile rarefaction wave is formed that can cause spallation<sup>38</sup> of the material within the upper cone of the crater if the tensile material strength is exceeded. The melting process does not reach the surface in this case [see Fig. 22(f)], but still facilitates spallation by reducing material strength in the central part of the crater. The described crater morphologies and corresponding processes appeared to be consistent for a wide (more than an order-of-magnitude) range of gold absorber sizes and lodging depths. Craters produced by 19-nm gold particles with a lodging depth ranging from 30 to 240 nm (shown in Fig. 22) are qualitatively similar to craters initiated by 600-nm gold particles at 2- $\mu\text{m}$  and 5- $\mu\text{m}$  lodging depths<sup>39,40</sup> (shown in Fig. 23). Comparison with theory shows qualitative agreement for 600-nm particles between experiment [Figs. 23(a) and (b)] and finite-element modeling [Figs. 23(c) and (d)] using *DELPOR* and *HESIONE* codes previously described in Sec. 2.4. On the other hand, crater lateral-size predictions using scaling relations between lateral size and absorber lodging depth<sup>29</sup> disagree with experiments (see Sec. 3.5, Fig. 17) due to significant growth in crater lateral size when the spallation process turns on at deeper absorber locations.

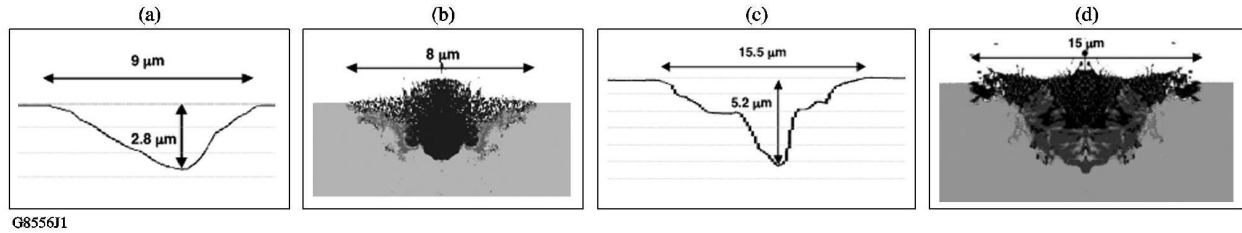


Fig. 23. Damage craters produced by a 355-nm, 3-ns, 6-J/cm<sup>2</sup> irradiation of 600-nm inclusion embedded in silica: (a) and (b) at 2- $\mu$ m depth (after Bonneau *et al.*<sup>39</sup>); (c) and (d) at 5- $\mu$ m depth (after Bercegol *et al.*<sup>40</sup>); (a) and (c) experimental AFM measurements; (b) and (d) finite element modeling.

Surface-damage morphology of the fused-silica glass finished according to fusion-scale laser specifications and irradiated by nanosecond pulses at 355-nm wavelength<sup>41</sup> reveals features similar to those observed in the model systems. A large,  $\sim$ 50- $\mu$ m-diam crater shown in Fig. 24 has a clearly melted central core [Fig. 24(b)] and periphery formed through fracture, most probably spallation. Cross-sectional analysis [Fig. 24(c)] shows that energy deposited in the melted core was not enough to cause full material expulsion and the cooling stage of the moving up melt is finalized by central bump formation. Another example of the frequently observed fused-silica damage morphology is a small,  $\sim$ 1- $\mu$ m-diam crater [Fig. 24(d)] with features (symmetry, elevated rim) typical for explosive melting and evaporation, like a regular crater in the model systems.

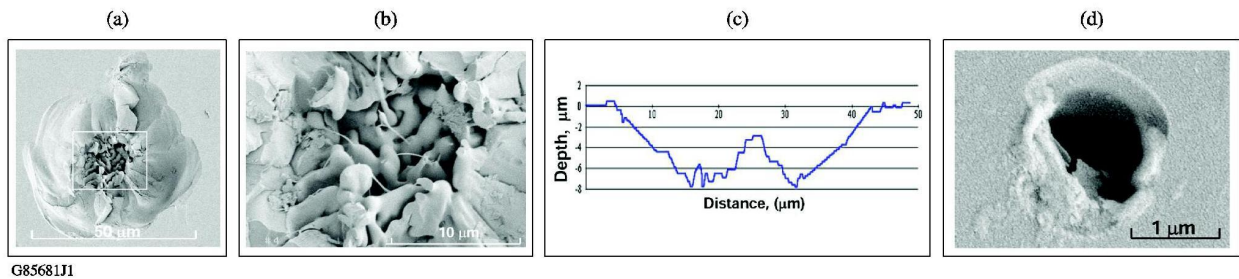


Fig. 24. Damage craters produced in fused silica by 355-nm, 7.5-ns pulse with 45-J/cm<sup>2</sup> fluence: (a) large crater with melted central core and fractured periphery; (b) magnified image of the central core; (c) cross-sectional profile of the crater shown in (a); (d) small craters produced by melting and evaporation (after Wong *et al.*<sup>41</sup>).

### 3.8 Structural modification of the damaged-glass material and damage growth under conditions of consecutive pulsed irradiation

Detailed structural analysis<sup>41–43</sup> of the material inside damage craters, similar to those shown in Fig. 24(a), revealed significant structural modification of damaged material. A schematic of the crater cross section highlighting the main features of crater morphology<sup>41</sup> responsible for damage growth is given in Fig. 25. The crater floor and wall (molten core) contain a  $\sim$ 10- $\mu$ m-thick and  $\sim$ 20% compacted, strained layer with a high concentration of oxygen-deficient centers and self-trapped excitons, where energy from UV pulses may be effectively absorbed. Morphology in the form of cracks is represented by a concentric fractured shell, where non-bridging oxygen hole centers are found, and by different sized (micro- and nanoscale) open and closed radial cracks. Experimental studies confirmed that crack propagation is the main mechanism of damage growth when such craters are exposed to consecutive nanosecond laser pulses.<sup>44</sup> Moreover, damage sites located at the entrance surface show linear growth with a number of 351-nm pulses, in contrast to clearly exponential exit-surface-damage growth (see Fig. 26). Lateral- and side-view morphology of damage sites grown to

~2 mm depicted in Fig. 27 show much deeper crack propagation in the case of exit surface compared to the entrance surface case. The difference is qualitatively explained, as illustrated schematically in Fig. 28, by high pressures associated with plasma formation inside material during exit-surface irradiation. In the entrance-surface case, plasma expands outward and partially screens surface material from radiation, leading to smaller damage extent.

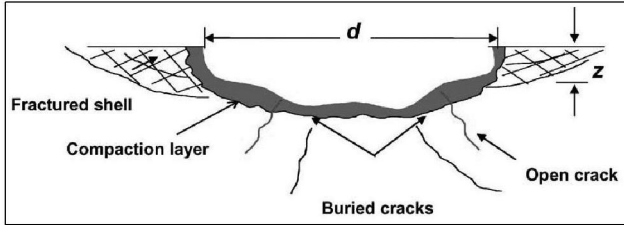


Fig. 25. Schematics of damage-crater morphology (after Wong *et al.*<sup>41</sup>).

G8560J1

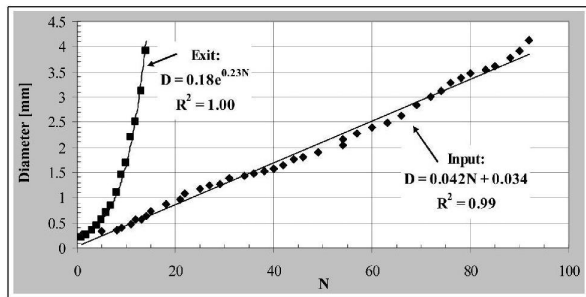
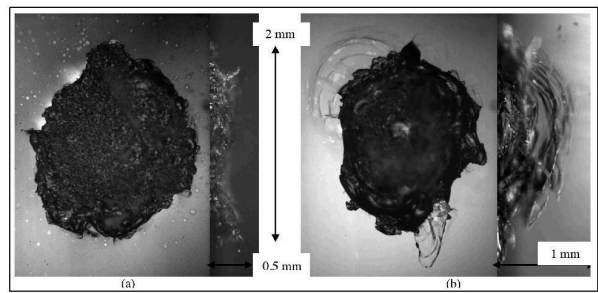


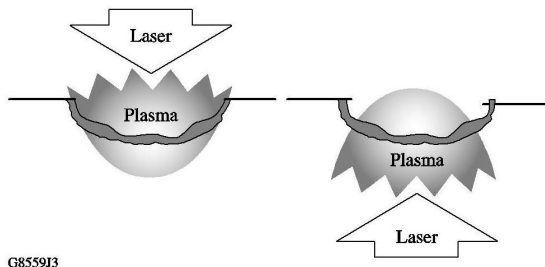
Fig. 26. Damage growth on fused-silica entrance and exit surfaces under repetitive irradiation with 351-nm, 11-ns, 10-J/cm<sup>2</sup> pulses (after Norton *et al.*<sup>44</sup>).

G8559J1



G8559J2

Fig. 27. Top and side views of damage craters grown to millimeter-scale size: (a) on the entrance surface; (b) on the exit surface (after Norton *et al.*<sup>44</sup>).



G8559J3

Fig. 28. Schematic illustration of the damage-plasma interaction with surface material during entrance- and exit-surface irradiation.

### 3.9 Entrance-surface versus exit-surface damage

A standard approach<sup>45,46</sup> based on E-field intensity ( $\sim E^2$ ) calculations, taking into account interference between incident and reflected waves at the material boundary, predicts the following exit-to-entrance surface  $T_{\text{exit}}/T_{\text{ent}}$  threshold ratio

$$T_{\text{exit}}/T_{\text{ent}} = (n+1)^2 / 4n^2, \quad (15)$$

which leads, for  $n > 1$ , to  $T_{\text{exit}} < T_{\text{ent}}$ . This well-known result statistically holds for most transparent dielectrics. Nevertheless, for glass materials with a >20-mm-thick nonlinear coherent volume, processes such as stimulated Brillouin scattering (SBS) can influence surface-damage thresholds by generating scattered waves with an intensity comparable

with incident wave. Experiments with fused silica<sup>47</sup> demonstrated that front-surface damage can be dominant in the case of coherent (single-mode) irradiation, as shown in Fig. 29(a), due to the stimulated backscattering process. On the other hand, using high-bandwidth, multimode pulses with reduced coherence causes SBS suppression and preferential exit-surface damage [see Fig. 29(b)]. Another case, when the relation between  $T_{\text{exit}}$  and  $T_{\text{ent}}$  may vary significantly, is attributed to the interaction with nanoscale absorbers (diam  $\square \lambda$ ) located at a particular depth beneath the surface, as shown in Fig. 30. In this experiment<sup>48</sup> 8-nm and 14-nm-diam gold nanoparticles were embedded in fused silica at 60-nm and 120-nm depths, respectively, corresponding to “min” and “max” of the standing wave E-field intensity in the back-irradiation configuration. Front irradiation corresponds to a traveling wave with constant intensity  $I_{\text{front}}$ , intermediate between  $I_{\text{back}}^{\text{max}}$  and  $I_{\text{back}}^{\text{min}}$ . Damage thresholds (351 nm, 0.5 ns) measured for such model system in front- and back-irradiation configurations ( $T_{\text{front}}$  and  $T_{\text{back}}$ , respectively) are presented in Table 1. One can see that thresholds qualitatively follow the E-field intensity changes inside the sample, particularly  $T_{\text{back}} > T_{\text{front}}$  for a 60-nm depth, where  $I_{\text{back}} < I_{\text{front}}$ , and  $T_{\text{back}} < T_{\text{front}}$  for a 120-nm depth, where  $I_{\text{back}} > I_{\text{front}}$ . An important observation here is that once normalized to internal intensity values ( $T_{\text{front}}^n = T_{\text{front}} \times I_{\text{front}} / I_0$ ,  $T_{\text{back}}^n = T_{\text{back}} \times I_{\text{back}} / I_0$ , where  $I_0$  is incident intensity), the back-irradiation thresholds show an  $\sim 20\%$  increase compared to the front-irradiation thresholds for both absorber locations (see Table 1). Such an increase in back-irradiation thresholds can be attributed to the asymmetry in

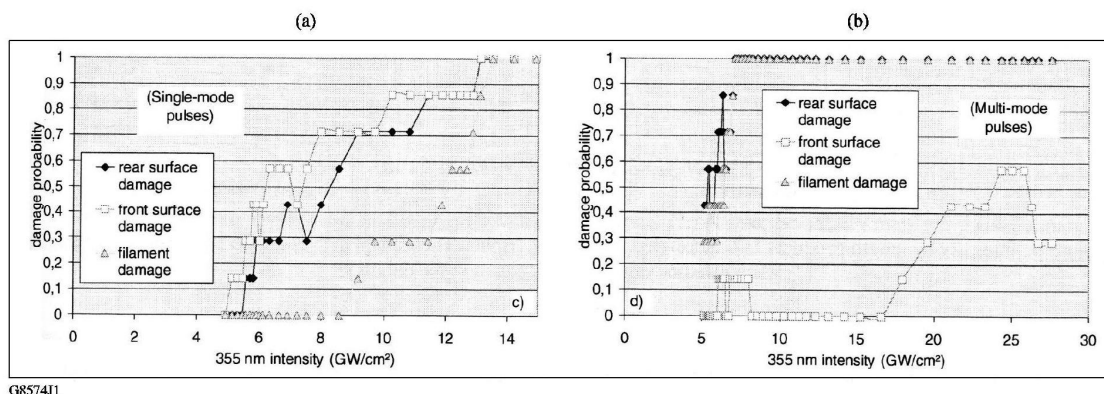


Fig. 29. Fused-silica damage-probability plots for 355-nm pulsed irradiation: (a) single-mode, 5.4-ns pulses; (b) multimode, 3.1-ns pulses (after Bercegol *et al.*<sup>47</sup>).

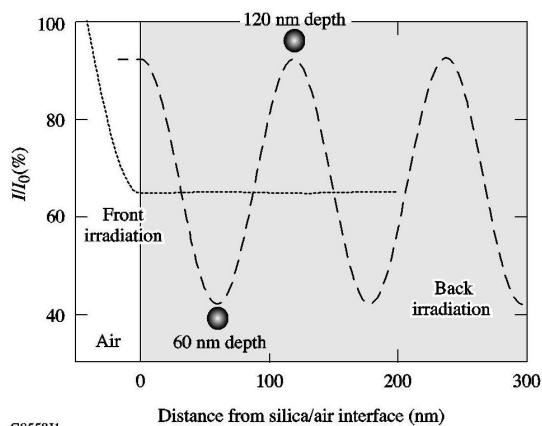


Fig. 30. E-field intensity distribution inside fused silica containing gold nanoparticles at fixed depth locations: 8-nm particles at 60-nm depth and 14-nm particles at 120-nm depth, corresponding to “min” and “max” of the back irradiation intensity, respectively.<sup>48</sup>

plasma-ball growth as illustrated in Fig. 31. Since plasma-ball growth implies that laser radiation is being absorbed by the plasma, it is clear that sample areas behind the plasma front are partially screened from laser radiation, which should cause a departure from spherical symmetry and preferential plasma growth toward the laser-beam source. In such a scenario, front irradiation generates plasma preferentially growing toward the glass/air interface, thus facilitating damage crater formation (see Fig. 31). On the contrary, back irradiation causes plasma propagation away from the glass surface, which reduces the probability of crater formation. One can see that the effect is not dramatic and can be easily overshadowed by the effects of internal E-field distribution.

Table 1. Front- and back-irradiation thresholds for the model system with gold absorbers shown in Fig. 30. Thresholds  $T_{\text{front}}^n$  and  $T_{\text{back}}^n$  are normalized to sample internal intensity values using  $I/I_0$  factor.

Particle diam/location	Threshold J/cm <sup>2</sup>		Normalized threshold J/cm <sup>2</sup>		Threshold ratio
	$T_{\text{front}}$	$T_{\text{back}}$	$T_{\text{front}}^n$	$T_{\text{back}}^n$	$T_{\text{back}}^n / T_{\text{front}}^n$
8 nm, 60 nm, $E_{\text{low}}$	1.140.08	2.14±0.13	0.74±0.05	0.90±0.05	1.21±0.11
14 nm, 120 nm, $E_{\text{high}}$	0.63±0.11	0.55±0.06	0.41±0.07	0.51±0.06	1.24±0.28

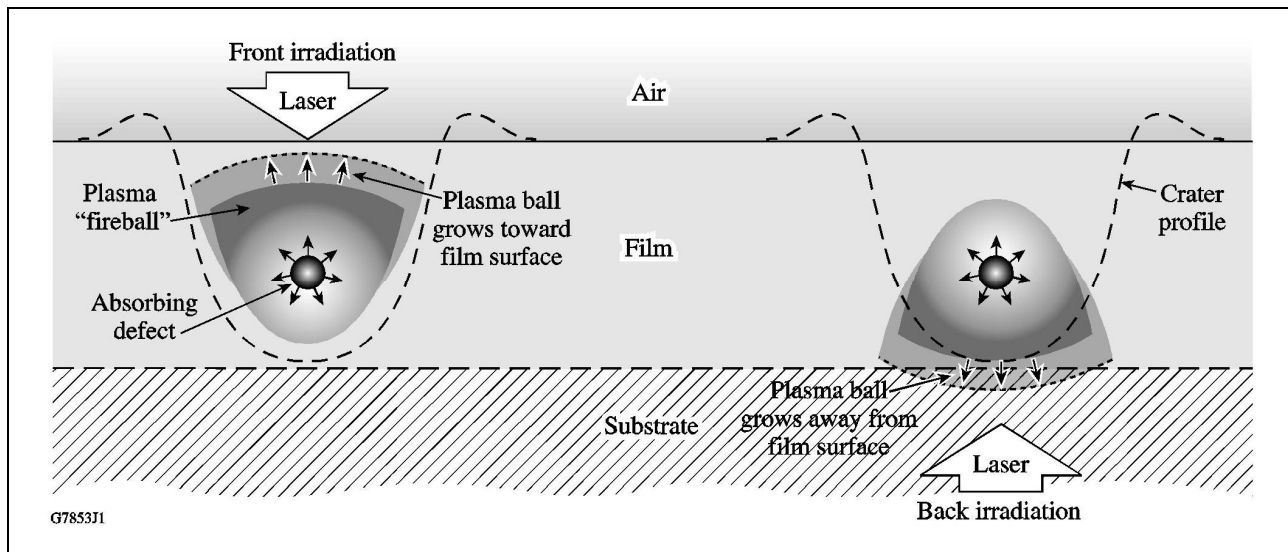


Fig. 31. Illustration of the impact that plasma-ball growth symmetry has on crater formation for front-back-irradiation geometries.<sup>48</sup>

### 3.10 Surface damage initiated by adsorbed metallic particles

Surface contamination is one of the processes leading to the degradation of high-power laser optics, and contamination by highly absorbing metal particles is especially dangerous. Interaction of pulsed-laser radiation with these particles is usually accompanied by the plasma formation with subsequent energy deposition in the underlying substrate leading to damage. Using model systems with well-characterized metallic contaminants also proved to be instrumental in this case.<sup>49–52</sup> Different behavior was observed for 1- $\mu\text{m}$ -thick circular Al dots (10- to 250- $\mu\text{m}$  diameter) deposited on entrance and exit surfaces of the fused-silica sample<sup>49</sup> and irradiated by nanosecond pulses at 1064-nm and 355-nm wavelengths. In the case of the entrance-surface contamination and 1064-nm pulses, minor damage in the form of small isolated craters was observed after the first shot with moderate fluence, characterized by partial dot melting, evaporation, and material redeposition around the dot. Subsequent pulses also interacted with redeposited material with the eventual

saturation in damage size scaling to  $\sim 3\times$  the initial dot size. In the case of exit-surface contamination, damage usually is produced on the first shot, confined to the dot location (scales as  $\sim 1.4\times$  dot size), and does not grow after being subjected to subsequent laser pulses. Irradiation by 355-nm pulses, as compared to 1064 nm, caused much stronger, frequently catastrophic damage. The most striking feature was frequent strong damage on the exit surface when the Al dot was located at the entrance surface. Parallel studies<sup>50</sup> showed that diffraction of the incident beam on the Al dot caused intensity modulation and damage at the exit surface. Modeling done in the same work<sup>50</sup> also suggested that the difference in damage behavior for Al dots located at the entrance and exit surfaces is linked to plasma characteristics. In the case of exit surface, plasma is confined between the Al dot and substrate, and generates much higher (compared to the entrance-surface case) pressures that can easily cause ejection of the dot. This result points to the possibility of metal contamination removal without damage by finding the appropriate laser fluence—well known as laser cleaning. Such tuning of the irradiation regime was successfully demonstrated<sup>52</sup> using similar artificial Al dot contamination ( $5 \times 5 \times 1 \mu\text{m}$  or  $50 \times 50 \times 1 \mu\text{m}$  squares, see Fig. 32) on the exit surface of the fused-silica sample. This study, complemented by photothermal microscopy measurements, allowed us to link the damage process under repetitive 1064-nm, 6.5-ns pulse irradiation to residual absorption caused by redeposition of the Al material. It was found that the first shot fluence is of critical importance in achieving the cleaning regime. Images presented in Fig. 33 show that ten irradiations of the 50- $\mu\text{m}$  Al squares with high, 40-J/cm<sup>2</sup> fluence incur catastrophic damage, while one shot at 5 J/cm<sup>2</sup> plus 100 shots at 40 J/cm<sup>2</sup> cause much smaller and stable (relative to consecutive irradiation) damage. Finally, one shot at 15 J/cm<sup>2</sup> plus 100 shots at 40 J/cm<sup>2</sup> caused only a small  $\sim 200\text{-nm}$  depression on the fused-silica surface, which is very stable under 40-J/cm<sup>2</sup> multiple irradiation.

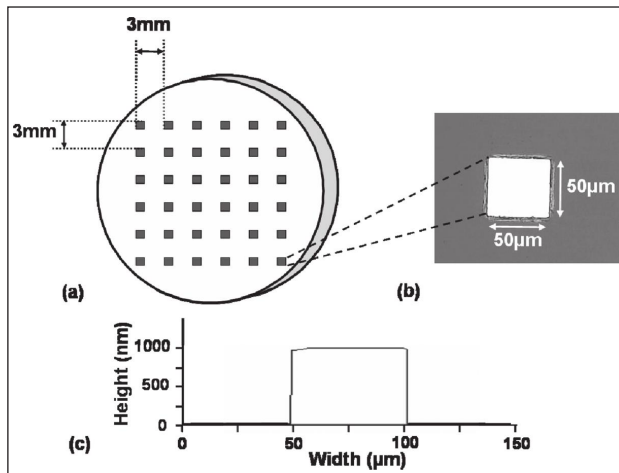
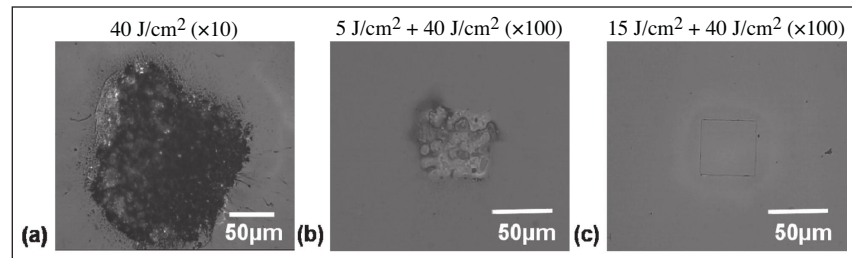


Fig. 32. Schematics of the fused-silica sample with 50- $\mu\text{m}$  square Al dots (after Palmier *et al.*<sup>52</sup>).

G8557J1



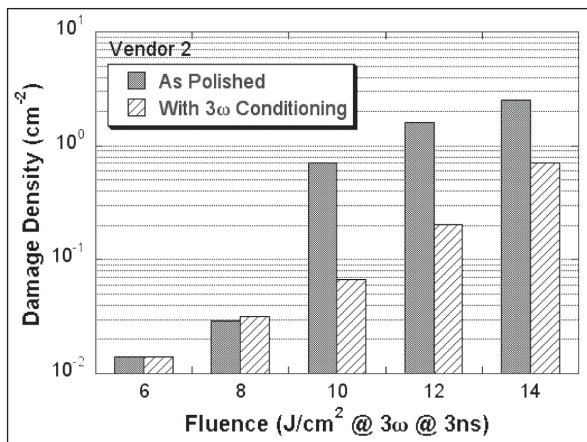
G8557J2

Fig. 33. Images of 1064-nm, 6.5-ns damage generated at three 50- $\mu\text{m}$  Al dot locations on the fused-silica sample exit surface: (a) 10 shots at 40 J/cm<sup>2</sup>; (b) 1 shot at 5 J/cm<sup>2</sup> plus 100 shots at 40 J/cm<sup>2</sup>; (c) 1 shot at 15 J/cm<sup>2</sup> plus 100 shots at 40 J/cm<sup>2</sup> (after Palmier *et al.*<sup>52</sup>).

## 4. METHODS OF IMPROVING SURFACE-DAMAGE RESISTANCE OF TRANSPARENT DIELECTRICS

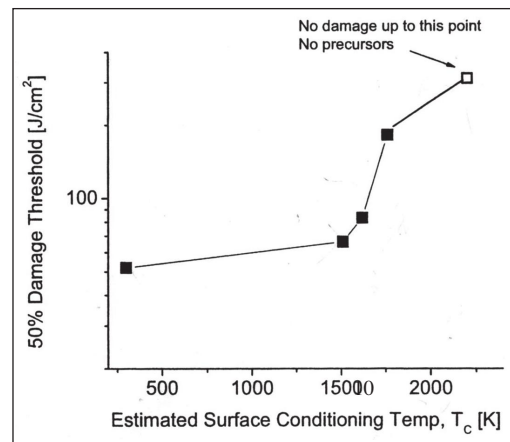
### 4.1 Laser-conditioning effects

Although mechanisms of improving damage thresholds of bare surfaces, bulk materials, and thin films by laser irradiation at sub-threshold fluence is not very well understood, this technique is widely used to prolong the life of optics for high-power lasers. One of the possible conditioning mechanisms, discussed in Sec. 3.6 in the context of localized absorber-driven damage, may be dispersion of the absorber into smaller constituents with subsequent diffusion into the surrounding matrix. Such a process reduces local energy density deposited during exposure to higher, potentially damaging laser fluence, therefore improving damage resistance. One example of highly effective UV-laser conditioning of the polished fused-silica surfaces<sup>53</sup> is presented in Fig. 34, showing results of sample damage testing with and without conditioning. The conditioning (355 nm, 7.5 ns) was done by sample raster scanning with 50% beam overlap, fluence ramp of 4 J/cm<sup>2</sup>, 6 J/cm<sup>2</sup>, and 8 J/cm<sup>2</sup>, three times for each fluence level. One can find that, starting from the testing fluence of 10 J/cm<sup>2</sup>, an order-of-magnitude reduction in damage-site density is achieved by applying laser conditioning. Another type of fused-silica conditioning recently explored is thermal conditioning,<sup>37</sup> when local surface heating up to ~2200 K by a CO<sub>2</sub> laser allows one to achieve a factor-of-6 increase in 355-nm, 7-ns damage thresholds (see Fig. 35). The feasibility of this conditioning technique is yet to be proved, since the impact of partial melting of the material at such high temperatures and of stresses induced by thermal cycling have to be quantified.



G8567J1

Fig. 34. Damage density versus 355-nm, 3-ns fluence for polished fused-silica surface, with and without UV-laser conditioning (after Brusasco *et al.*<sup>53</sup>).



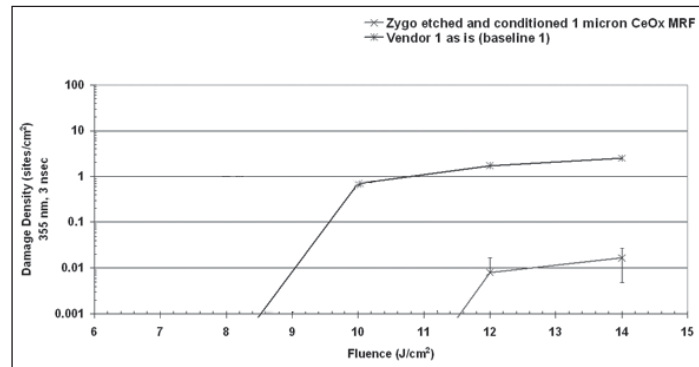
G8567J2

Fig. 35. Fused-silica surface 355-nm, 7.5-ns thresholds as a function of surface temperature (after Bude *et al.*<sup>37</sup>).

### 4.2 Advanced surface processing

Earlier discussions (see Sec. 3.1) pointed out that major sources of absorption (subsurface damage, etc.) in the glass near-surface layer are usually introduced during the surface-finishing process. Recently, a sequence of additional technological steps was suggested<sup>54</sup> that made it possible to remove the modified absorbing layer without compromising the surface figure. These steps include magnetorheological (MRF) finishing,<sup>55</sup> HF acid etching, and UV-laser conditioning. The MRF process is based on polishing by a ribbon of liquid containing a mixture of magnetic and abrasive particles attracted to the workpiece by a magnetic field. This process produces much smaller local normal pressure than in conventional lap polishing and allows removal of the modified surface layer without introducing additional structural damage. Nevertheless, to achieve further improvement in the UV damage thresholds, the chemically

modified top layer requires removal by acid etching, followed by UV-laser conditioning. As a result (see Fig. 36), two-orders-of-magnitude reduction in 355-nm, 3-ns damage density has been achieved for fused-silica material.<sup>54</sup>



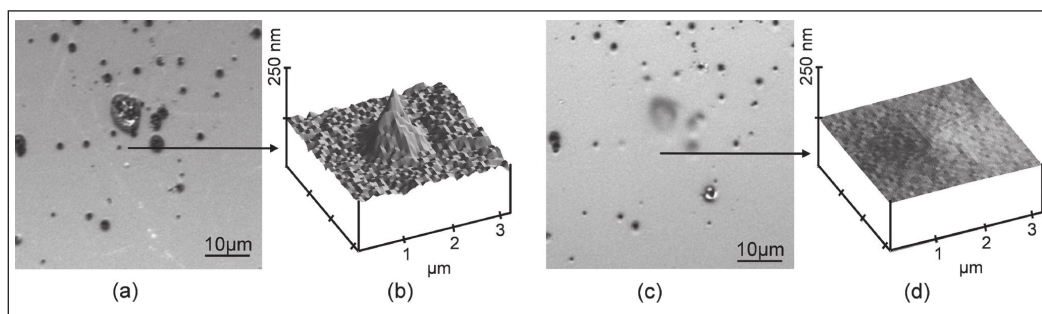
G8565J1

Fig. 36. Damage density versus 355-nm, 3-ns fluence for conventionally polished fused-silica surface and surface additionally subjected to MRF finishing, HF acid etching, and UV-laser conditioning (after Menapace *et al.*<sup>54</sup>).

## 5. MITIGATION OF DIELECTRIC SURFACE DAMAGE

### 5.1 Mitigation using a CO<sub>2</sub> laser

Surface-damage-growth mitigation is essential for the lifetime extension of very expensive large-scale laser optics. The main method for repairing damaged glass optics is remelting damaged sites using an infrared CO<sub>2</sub> laser in the cw or pulsed regime. It was demonstrated<sup>56</sup> that small-scale damage (1- to 5- $\mu$ m-diam,  $\sim$ 1- $\mu$ m-deep craters) can be mitigated in fused silica using 10.6- $\mu$ m radiation in the subablation, melting regime. An example of such mitigation using single 10.6- $\mu$ m, 200-ms pulses is shown in Fig. 37, where a  $\sim$ 170-nm-deep crater in fused silica is converted after remelting into a smooth, shallow ( $\sim$ 8-nm-deep) pit. A more-elaborate procedure is required for the mitigation of large,  $>100$ - $\mu$ m-diam and several 10- $\mu$ m-deep craters by 10.6- $\mu$ m radiation due to a relatively small ( $\sim$ 40- $\mu$ m) absorption length in fused silica. Mitigation of such craters in glass requires significant material removal to heal deeply propagating subsurface cracks and is usually done using the ablative regime of irradiation by a 10.6- $\mu$ m CO<sub>2</sub> laser. The mitigation process involves spiral-type raster scanning<sup>57</sup> of the laser beam ( $\sim$ 200- $\mu$ m spot, 5-kHz pulse frequency) over the damaged site with a carefully adjusted pulse width (10- $\mu$ s to cw). Figure 38 shows a  $\sim$ 300- $\mu$ m-diam damage site, which, after



G8563J1

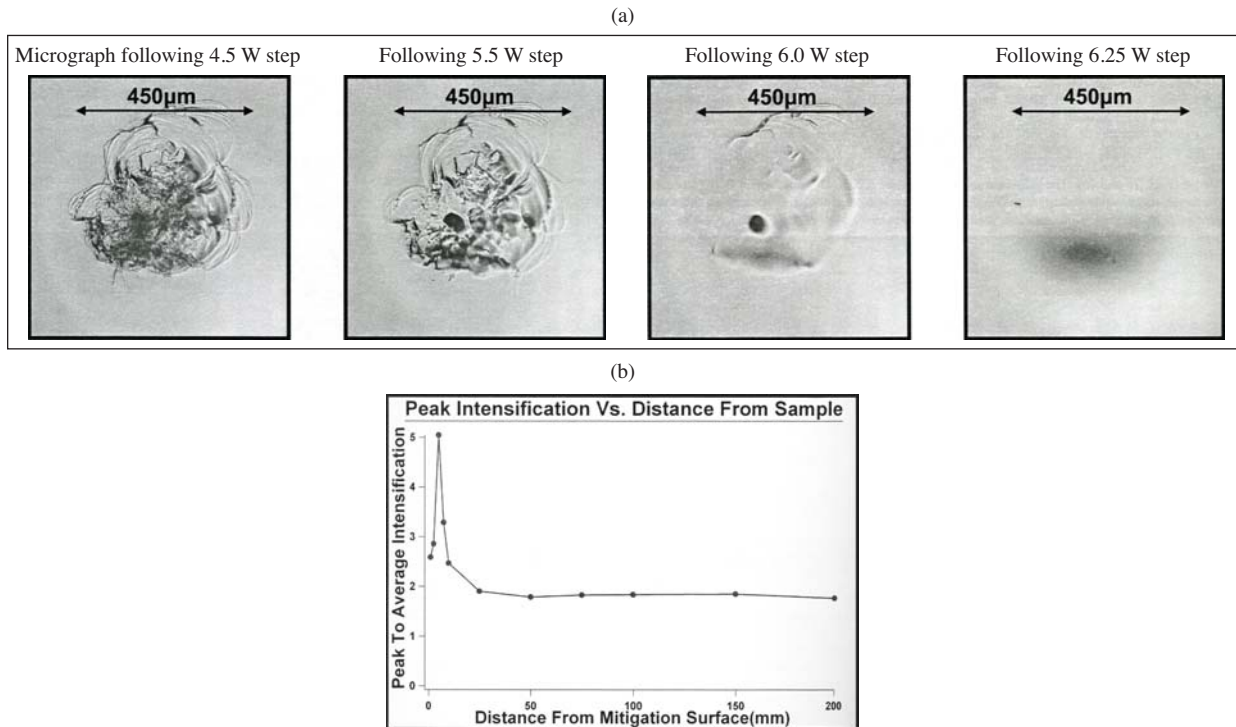
Fig. 37. Small-scale damage mitigation using a 10.6- $\mu$ m CO<sub>2</sub> laser in the melting regime: (a) damaged site before mitigation; (c) after mitigation with a single 200-ms pulse; (b) and (d) show corresponding high-resolution AFM images (inverted) of isolated mitigated pit (after Mendez *et al.*<sup>56</sup>).



G8562J1

Fig. 38. Large-scale mitigation using a 10.6- $\mu\text{m}$  CO<sub>2</sub> laser in the ablative regime. The largest (360  $\mu\text{m}$   $\times$  260  $\mu\text{m}$ ) mitigated site survived 355-nm, 7.5-ns raster-scan testing with 22-J/cm<sup>2</sup> fluence (after Bass *et al.*<sup>57</sup>).

mitigation, survived 355-nm, 7.5-ns testing with 22-J/cm<sup>2</sup> fluence. The drawback of this mitigation technique is the formation of rather deep (as deep as subsurface cracks are,  $\sim 60$   $\mu\text{m}$  in the described case) pits causing danger for downstream optic-light intensification. To overcome this difficulty, 4.6- $\mu\text{m}$  wavelength of a CO<sub>2</sub> laser which had an  $\sim 25\times$  longer absorption length in fused silica, compared to 10.6- $\mu\text{m}$  wavelength, was recently utilized.<sup>58</sup> Using 4.6- $\mu\text{m}$ , 22-ns pulses with a 75-kHz repetition rate (maximum average power 6.5 W) allowed the mitigation of damage craters of up to 500- $\mu\text{m}$  size and 200- $\mu\text{m}$  depth in a pure melting (subablation) regime [see Fig. 39(a)]. Measured downstream intensification from mitigated sites presented in Fig. 39(b) shows an acceptable level, as per National Ignition Facility requirements, at distances  $>10$  mm. Testing of the mitigated sites established a 355-nm, 7.5-ns threshold of 25 J/cm<sup>2</sup>.



G8561J1

Fig. 39. Mitigation by a 4.6- $\mu\text{m}$  CO<sub>2</sub> laser in the melting regime: (a) microscope images show surface morphology after each step of the four-step power-ramp procedure (b) laser-beam peak intensity as a function of distance from the mitigated surface (after Guss *et al.*<sup>58</sup>).

## 5.2 Mitigation using single-crystal diamond micromachining

For crystalline material optics, like KDP/DKDP frequency-conversion crystals, another pure mechanical mitigation method using micromachining with a high-speed motor and single-crystal diamond bit was implemented.<sup>59</sup> It was shown that dimples created with such a tool on an undamaged KDP surface can withstand 527-nm, 3.2-ns pulses with fluences up to 14 J/cm<sup>2</sup>. In the case of DKDP and 351-nm, 3-ns pulses, dimples are damage resistant to fluences up to 10 J/cm<sup>2</sup>. Dimples created on damaged DKDP sites also showed excellent resistance to 351-nm irradiation. Only one out of 24 sites failed after being subjected to fluences in the range of 8 to 10 J/cm<sup>2</sup>, and two sites tested for multiple-shot effects using 351-nm, 11-ns pulses survived 600-shot, 12 J/cm<sup>2</sup> irradiation (see Fig. 40).

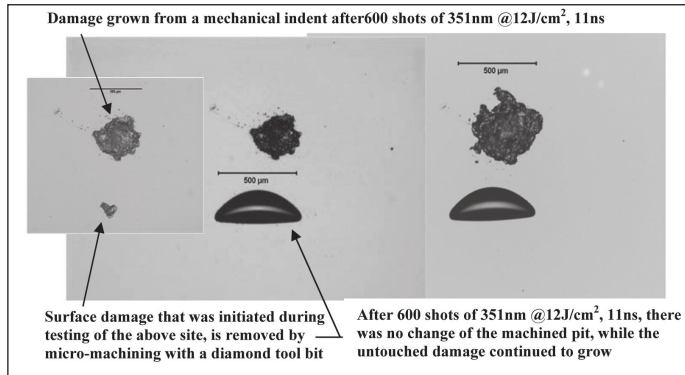


Fig. 40. Mitigation of damage on the DKDP crystal surface using diamond-tool micromachining (after Hrubesh *et al.*<sup>59</sup>).

## 6. CONCLUSIONS

Significant progress has been made in both understanding the physics of laser-induced damage to optical material surfaces and increasing surface-damage resistance through more sophisticated technological processing.

New, recently developed techniques for surface laser conditioning, contamination removal, and damage mitigation makes it possible to significantly extend the lifetime of optical components in high-power laser systems.

Further challenges, related to ever-increasing laser-power densities, can be met only through better understanding of surface-damage mechanisms. Progress in detailed theoretical modeling of extrinsically and intrinsically driven damage is currently hampered by a lack of information about material properties at elevated temperatures and pressures. Generation of such information is of crucial importance.

An experimental challenge to overcome is the characterization of micro- and nanoscale absorbers distributed with very low densities in the near-surface layer. It requires dramatic improvement in sensitivity of existing (photothermal, for instance) techniques and even an introduction of new methods.

## ACKNOWLEDGMENT

This work was supported by the U.S. Department of Energy Office of Inertial Confinement Fusion under Cooperative Agreement No. DE-FC52-08NA28302, the University of Rochester, and the New York State Energy Research and Development Authority. The support of DOE does not constitute an endorsement by DOE of the views expressed in this article.

## REFERENCES

1. J. A. Dobrowolski, "Coatings and filters," in *Handbook of Optics*, edited by W. G. Driscoll and W. Vaughan, Sec. 8, p. 8-92, Fig. 97, McGraw-Hill, New York, 1978.
2. W. L. Wolfe, "Properties of optical materials," in *Handbook of Optics*, edited by W. G. Driscoll and W. Vaughan, Sec. 7, p. 7-60, Fig. 156, McGraw-Hill, New York, 1978.
3. Y. Jee, M. F. Becker, and R. M. Walser, "Damage morphologies and cumulative behavior of laser damage on single crystal metal surfaces," in *Damage in Laser Materials: 1986*, edited by H. E. Bennett, A. H. Guenther, D. Milam, and B. E. Newnam, NIST (U.S.) Special Publication 752, pp. 575-593, SPIE, Bellingham, WA, 1987.
4. Y. Jee, M. F. Becker, and R. M. Walser, "N-on-1 damage testing of single crystal metal surfaces at 1.06  $\mu\text{m}$ ," in *Damage in Laser Materials: 1985*, edited by H. E. Bennett, A. H. Guenther, D. Milam, and B. E. Newnam, Nat. Bur. Stand. (U.S.), Spec. Publ. 746, pp. 236-247, U.S. Government Printing Office, Washington, DC, 1987.
5. H. M. Musal, Jr., "Pulsed laser initiation of surface plasma on metal mirrors," in *Damage in Laser Materials: 1980*, edited by H. E. Bennett, A. J. Glass, and A. H. Guenther, Natl. Bur. Stand. (U.S.), Spec. Publ. 746, pp. 227-237, U.S. Government Printing Office, Washington, DC, 1981.
6. J. O. Porteus, D. L. Decker, D. J. Grandjean, S. C. Seitel, and W. N. Faith, "Defect-damage-resistant copper mirrors," in *Damage in Laser Materials: 1979*, edited by H. E. Bennett, A. J. Glass, and A. H. Guenther, Nat. Bur. Stand. (U.S.), Spec. Publ. 568, pp. 175-186, U.S. Government Printing Office, Washington, DC, 1979.
7. S. R. J. Brueck and D. J. Ehrlich, "Stimulated surface-plasma-wave scattering and growth of a periodic structure in laser-photodeposited metal films," *Phys. Rev. Lett.* **48**(24), 1678-1681 (1982).
8. J. F. Young, J. S. Preston, H. M. van Driel, and J. E. Sipe, "Laser-induced periodic surface structure. II. Experiments on Ge, Si, Al, and brass," *Phys. Rev. B* **27**(2), 1155-1172 (1983).
9. N. Mansour, G. Reali, P. Aiello, and M. J. Soileau, "Laser generated ripple patterns on dielectrics and intermediate band gap semiconductors," in *Damage in Laser Materials: 1984*, edited by H. E. Bennett, A. H. Guenther, D. Milam, and B. E. Newnam, Nat. Bur. Stand. (U.S.), Spec. Publ. 727, pp. 137-146, U.S. Government Printing Office, Washington, DC, 1986.
10. Z. Guosheng, P. M. Fauchet, and A. E. Siegman, "Growth of spontaneous periodic surface structures on solids during laser illumination," *Phys. Rev. B* **26**(10), 5366-5381 (1982).
11. C. S. Lee, N. Koumvakalis, and M. Bass, "Spot-size dependence of laser-induced damage to diamond-turned Cu mirrors," *Appl. Phys. Lett.* **41**(7), 625-627 (1982).
12. J. Hue, J. DiJon, and P. Lyan, "Thermal behavior of optical mirrors under high-power continuous wave CO<sub>2</sub> laser irradiation," in *Laser-Induced Damage in Optical Materials: 1992*, edited by H. E. Bennett, L. L. Chase, A. H. Guenther, B. E. Newnam, and M. J. Soileau, Vol. 1848, pp. 125-137, SPIE, Bellingham, WA, 1993.
13. R. Fedosejevs, S. E. Kirkwood, R. Hostenstein, N. Young, and Y. Y. Tsui, "Femtosecond interaction processes near threshold: Damage and ablation," in *Laser-Damage in Optical Materials: 2006*, edited by G. J. Exarhos, A. H. Guenther, K. L. Lewis, D. Ristau, M. J. Soileau, and C. J. Stolz, Vol. 6403, p. 640302, SPIE, Bellingham, WA, 2007.
14. S. Nolte, C. Momma, H. Jacobs, A. Tünnermann, B. N. Chichkov, B. Wellegehausen, and H. Welling, "Ablation of metals by ultrashort laser pulses," *J. Opt. Soc. Am. B* **14**(10), 2716-2722 (1997).
15. P. E. Miller, T. I. Suratwala, L. L. Wong, M. D. Feit, J. A. Menapace, P. J. Davis, and R. A. Steele, "The distribution of subsurface damage in fused silica," in *Laser-Induced Damage in Optical Materials: 2005*, edited by G. J. Exarhos, A. H. Guenther, K. L. Lewis, D. Ristau, M. J. Soileau, and C. J. Stolz, Vol. 5991, p. 599101, SPIE, Bellingham, WA, 2006.
16. R. W. Hopper and D. R. Uhlmann, "Mechanism of inclusion damage in laser glass," *J. Appl. Phys.* **41**(10), 4023-4037 (1970).
17. T. W. Walker, A. H. Guenther, and P. Nielsen, "Pulsed laser-induced damage to thin-film optical coatings—Part II: Theory," *IEEE J. Quantum Electron.* **QE-17**(10), 2053-2065 (1981).
18. M. Z. Fuka, J. K. McIver, and A. H. Guenther, "Effects of thermal conductivity and index of refraction variation on the inclusion dominated model of laser-induced damage," in *Laser Induced Damage in Optical Materials: 1989*, edited by A. J. Bennett, L. L. Chase, A. H. Guenther, B. E. Newnam, and M. J. Soileau, Vol. 1438, NIST Special Publication 801, pp. 576-583, SPIE, Bellingham, WA, 1990.

19. M. D. Feit and A. M. Rubenchik, "Implications of nanoabsorber initiators for damage probability curves, pulselength scaling, and laser conditioning," in *Laser-Induced Damage in Optical Materials: 2003*, edited by G. J. Exarhos, A. H. Guenther, N. Kaiser, K. L. Lewis, M. J. Soileau, and C. J. Stolz, Vol. 5273, pp. 74–82, SPIE, Bellingham, WA, 2004.
20. F. Bonneau, P. Combis, J. Vierne, and G. Daval, "Simulations of laser damage of SiO<sub>2</sub> induced by a spherical inclusion," in *Laser-Induced Damage in Optical Materials: 2000*, edited by G. J. Exarhos, A. H. Guenther, M. R. Kozlowski, K. L. Lewis, and M. J. Soileau, Vol. 4347, pp. 308–315, SPIE, Bellingham, WA, 2001.
21. G. Mie, "Beiträge zur optik trüber medien, speziell kolloidaler metallosungen," *Ann. Phys.* **25**(3), 377–445 (1908); C. F. Bohren and D. R. Huffman, *Absorption and Scattering of Light by Small Particles*, Wiley, New York, 1983.
22. S. R. Foltyn, "Spotsize effects in laser damage testing," in *Damage in Laser Materials: 1982*, edited by H. E. Bennett, A. H. Guenther, D. Milam, and B. E. Newnam, Nat. Bur. Stand. (U.S.), Spec. Publ. 669, pp. 368–379, U.S. Government Printing Office, Washington, DC, 1984.
23. J. O. Porteus and S. C. Seitel, "Absolute onset of optical surface damage using distributed defect ensembles," *Appl. Opt.* **23**(21), 3796–3805 (1984).
24. R. M. O'Connell, "Onset threshold analysis of defect-driven surface and bulk laser damage," *Appl. Opt.* **31**(21), 4143–4153 (1992).
25. J.-Y. Natoli, L. Gallais, H. Akhouayri, and C. Amra, "Laser-induced damage of materials in bulk, thin-film, and liquid forms," *Appl. Opt.* **41**(16), 3156–3166 (2002).
26. H. Krol, L. Gallais, C. Grèzes-Besset, and J.-Y. Natoli, "Investigation of nanoprecursors threshold distribution in laser-damage testing," *Opt. Commun.* **256**, 184–189 (2005).
27. M. D. Feit, J. H. Campbell, D. R. Faux, F. Y. Genin, M. R. Kozlowski, A. M. Rubenchik, R. A. Riddle, A. Salleo, and J. Yoshiyama, "Modeling of laser-induced surface cracks in silica at 355 nm," in *Laser-Induced Damage in Optical Materials: 1997*, edited by G. J. Exarhos, A. H. Guenther, M. R. Kozlowski, and M. J. Soileau, Vol. 3244, pp. 350–355, SPIE, Bellingham, WA, 1998.
28. F. Bonneau, P. Combis, J. Vierne, and G. Daval, "Simulations of laser damage of SiO<sub>2</sub> induced by a spherical inclusion," in *Laser-Induced Damage in Optical Materials: 2000*, edited by G. J. Exarhos, A. H. Guenther, M. R. Kozlowski, K. L. Lewis, and M. J. Soileau, Vol. 4347, pp. 308–315, SPIE, Bellingham, WA, 2001.
29. M. D. Feit, L. W. Hrubesh, A. M. Rubenchik, and J. N. Wong, "Scaling relations for laser damage initiation craters," in *Laser-Induced Damage in Optical Materials: 2000*, edited by G. J. Exarhos, A. H. Guenther, M. R. Kozlowski, K. L. Lewis, and M. J. Soileau, Vol. 4347, pp. 316–323, SPIE, Bellingham, WA, 2001.
30. Yu. K. Danileiko, A. A. Manenkov, and V. S. Nechitailo, "The mechanism of laser-induced damage in transparent materials, caused by thermal explosion of absorbing inhomogeneities," *Sov. J. Quantum Electron.* **8**(1), 116–118 (1978).
31. S. Papernov and A. W. Schmid, "Two mechanisms of crater formation in ultraviolet-pulsed-laser irradiated SiO<sub>2</sub> thin films with artificial defects," *J. Appl. Phys.* **97**, 114906 (2005).
32. S. Papernov and A. W. Schmid, "Localized absorption effects during 351 nm, pulsed laser irradiation of dielectric multilayer thin films," *J. Appl. Phys.* **82**(11), 5422–5432 (1997).
33. J. Dijon, T. Poiroux, and C. Desrumaux, "Nano absorbing centers: A key point in laser damage of thin films," in *Laser-Induced Damage in Optical Materials: 1996*, edited by H. E. Bennett, A. H. Guenther, M. R. Kozlowski, B. E. Newnam, and M. J. Soileau, Vol. 2966, pp. 315–325, SPIE, Bellingham, WA, 1997.
34. S. Papernov and A. W. Schmid, "Correlations between embedded single gold nanoparticles in SiO<sub>2</sub> thin film and nanoscale crater formation induced by pulsed-laser radiation," *J. Appl. Phys.* **92**(10), 5720–5728 (2002).
35. F. Bonneau, P. Combis, J.-L. Rullier, J. Vierne, M. Pellin, M. Savina, M. Broyer, E. Cottancin, J. Tuaillon, M. Pellarin, L. Gallais, J.-Y. Natoli, M. Perra, H. Bercegol, L. Lamaignère, M. Loiseau, and J. T. Donohue, "Study of UV laser interaction with gold nanoparticles embedded in silica," *Appl. Phys. B* **75**(8), 803–815 (2002).
36. P. Grua, J. P. Morreeuw, H. Bercegol, G. Jonusauskas, and F. Vallée, "Electron kinetics and emission for metal nanoparticles exposed to intense laser pulses," *Phys. Rev. B* **68**, 035424 (2003).
37. J. Bude, G. M. Guss, M. Matthews, and M. L. Spaeth, "The effect of lattice temperature on surface damage in fused silica optics," in *Laser-Induced Damage in Optical Materials: 2007*, edited by G. J. Exarhos, A. H. Guenther, K. L. Lewis, D. Ristau, M. J. Soileau, and C. J. Stolz, Vol. 6720, p. 672009, SPIE, Bellingham, WA, 2007.

38. S. I. Kudryashov, S. D. Allen, S. Papernov, and A. W. Schmid, "Nanoscale laser-induced spallation in SiO<sub>2</sub> films containing gold nanoparticles" *Appl. Phys. B* **82**(4), 523–527 (2006).
39. F. Bonneau, P. Combis, J.-L. Rullier, J. Vierende, B. Bertussi, M. Commandré, L. Gallais, J.-Y. Natoli, I. Bertron, F. Malaise, and J. T. Donohue, "Numerical simulations for description of UV laser interaction with gold nanoparticles embedded in silica," *Appl. Phys. B* **78**(3–4), 447–452 (2004).
40. H. Bercegol, F. Bonneau, P. Bouchut, P. Combis, L. Gallais, L. Lamaignere, J.-Y. Natoli, J.-L. Rullier, and J. Vierende, "Comparison of numerical simulations with experiment on generation of craters in silica by a laser," in *Laser-Induced Damage in Optical Materials: 2002*, edited by G. J. Exarhos, A. H. Guenther, N. Kaiser, K. L. Lewis, M. J. Soileau, C. J. Stolz, A. Giesen, and H. Weber, Vol. 4932, pp. 297–308, SPIE, Bellingham, WA, 2003.
41. J. Wong, J. L. Ferriera, E. F. Lindsey, D. L. Haupt, I. D. Hutcheon, and J. H. Kinney, "Morphology and microstructure in fused silica induced by high fluence ultraviolet 3 $\omega$  (355 nm) laser pulses," *J. Non-Cryst. Solids* **352**, 255–272 (2006).
42. M. A. Stevens-Kalceff, A. Stesmans, and J. Wong, "Defects induced in fused silica by high fluence ultraviolet laser pulses at 355 nm," *Appl. Phys. Lett.* **80**(5), 758–760 (2002).
43. M. A. Stevens-Kalceff, "Distribution of defects induced in fused silica by ultraviolet laser pulses before and after treatment with a CO<sub>2</sub> laser," *J. Appl. Phys.* **97**(11), 113519 (2005).
44. M. A. Norton, E. E. Donohue, M. D. Feit, R. P. Hackel, W. G. Hollingsworth, A. M. Rubenchik, and M. L. Spaeth, "Growth of laser damage on the input surface of SiO<sub>2</sub> at 351 nm," in *Laser-Induced Damage in Optical Materials: 2006*, edited by G. J. Exarhos, A. H. Guenther, K. L. Lewis, D. Ristau, M. J. Soileau, and C. J. Stolz, Vol. 6403, p. 64030L, SPIE, Bellingham, WA, 2007.
45. M. D. Crisp, N. L. Boling, and G. Dubé, "Importance of Fresnel reflections in laser surface damage of transparent dielectrics," *Appl. Phys. Lett.* **21**(8), 364–366 (1972).
46. J. W. Arenberg, "Calculation of relative damage thresholds for total internal reflection surfaces," in *Laser-Induced Damage in Optical Materials: 2000*, edited by G. J. Exarhos, A. H. Guenther, M. R. Kozlowski, K. L. Lewis, and M. J. Soileau, Vol. 4347, pp. 324–335, SPIE, Bellingham, WA, 2001.
47. H. Bercegol, L. Lamaignère, V. Cavaro, and M. Loiseau, "Filamentation and surface damage in fused silica with single-mode and multi-mode pulses," in *Laser-Induced Damage in Optical Materials: 2005*, edited by G. J. Exarhos, A. H. Guenther, K. L. Lewis, D. Ristau, M. J. Soileau, and C. J. Stolz, Vol. 5991, p. 59911Z, SPIE, Bellingham, WA, 2006.
48. S. Papernov and A. W. Schmid, "Testing asymmetry in plasma-ball growth seeded by a nanoscale absorbing defect embedded in a SiO<sub>2</sub> thin-film matrix subjected to UV pulsed-laser radiation," *J. Appl. Phys.* **104**(6), 063101 (2008).
49. F. Y. Genin, K. Michlitsch, J. Furr, M. R. Kozlowski, and P. A. Krulevitch, "Laser-induced damage of fused silica at 355 nm and 1064 nm initiated at aluminum contamination particles on the surface," in *Laser-Induced Damage in Optical Materials: 1996*, edited by H. E. Bennett, A. H. Guenther, M. R. Kozlowski, B. E. Newnam, and M. J. Soileau, Vol. 2966, pp. 126–138, SPIE, Bellingham, WA, 1997.
50. M. D. Feit, A. M. Rubenchik, D. R. Faux, R. A. Riddle, A. B. Shapiro, D. C. Eder, B. M. Penetrante, D. Milam, F. Y. Genin, and M. R. Kozlowski, "Modeling of laser damage initiated by surface contamination," in *Laser-Induced Damage in Optical Materials: 1996*, edited by H. E. Bennett, A. H. Guenther, M. R. Kozlowski, B. E. Newnam, and M. J. Soileau, Vol. 2966, pp. 417–424, SPIE, Bellingham, WA, 1996.
51. S. Palmier, I. Tovenà, R. Courchinoux, M. A. Josse, J.-L. Rullier, B. Bertussi, J.-Y. Natoli, L. Servant, and D. Talaga, "Laser damage to optical components induced by surface chromium particles," in *Laser-Induced Damage in Optical Materials: 2004*, edited by G. J. Exarhos, A. H. Guenther, N. Kaiser, K. L. Lewis, and M. J. Soileau, Vol. 5647, pp. 156–164, SPIE, Bellingham, WA, 2005.
52. S. Palmier, J.-L. Rullier, J. Capoulade, and J.-Y. Natoli, "Effect of laser irradiation on silica substrate contaminated by aluminum particles," *Appl. Opt.* **47**(8), 1164–1170 (2008).
53. R. M. Brusasco, B. M. Penetrante, J. E. Peterson, S. M. Maricle, and J. A. Menapace, "UV-laser conditioning for reduction of 351-nm damage initiation in fused silica," in *Laser-Induced Damage in Optical Materials: 2001*, edited by G. J. Exarhos, A. H. Guenther, K. L. Lewis, M. J. Soileau, and C. J. Stolz, Vol. 4679, pp. 48–55, SPIE, Bellingham, WA, 2002.
54. J. A. Menapace, B. Penetrante, D. Golini, A. F. Slomba, P. E. Miller, T. G. Parham, M. Nichols, and J. Peterson, "Combined advanced finishing and UV-laser conditioning for producing UV-damage-resistant

- fused-silica optics,” in *Laser-Induced Damage in Optical Materials: 2001*, edited by G. J. Exarhos, A. H. Guenther, K. L. Lewis, M. J. Soileau, and C. J. Stolz, Vol. 4679, pp. 56–68, SPIE, Bellingham, WA, 2002.
55. S. D. Jacobs, D. Golini, Y. Hsu, B. E. Puchebner, D. Strafford, Wm. I. Kordonski, I. V. Prokhorov, E. Fess, D. Pietrowski, and V. W. Kordonski, “Magnetorheological finishing: A deterministic process for optics manufacturing,” in *Optical Fabrication and Testing*, edited by T. Kasai, Vol. 2576, pp. 372–382, SPIE, Bellingham, WA, 1995.
56. E. Mendez, K. M. Nowak, H. J. Baker, F. J. Villarreal, and D. R. Hall, “Localized CO<sub>2</sub> laser damage repair of fused silica optics,” *Appl. Opt.* **45**(21), 5358–5367 (2006).
57. I. L. Bass, G. M. Guss, and R. P. Hackel, “Mitigation of laser-damage growth in fused silica with a galvanometer scanned CO<sub>2</sub> laser,” in *Laser-Induced Damage in Optical Materials: 2005*, edited by G. J. Exarhos, A. H. Guenther, K. L. Lewis, D. Ristau, M. J. Soileau, and C. J. Stolz, Vol. 5991, p. 59910C, SPIE, Bellingham, WA, 2006.
58. G. Guss, I. L. Bass, V. Draggoo, R. Hackel, S. Payne, M. J. Lancaster, and P. Mak, “Mitigation of growth of laser initiated surface damage in fused silica using a 4.6- $\mu$ m wavelength laser,” in *Laser-Induced Damage in Optical Materials: 2006*, edited by G. J. Exarhos, A. H. Guenther, K. L. Lewis, D. Ristau, M. J. Soileau, and C. J. Stolz, Vol. 6403, p. 64030M, SPIE, Bellingham, WA, 2007.
59. L. W. Hrubesh, J. J. Adams, M. D. Feit, W. D. Sell, J. A. Stanley, E. Miller, S. L. Thompson, P. K. Whitman, and R. P. Hackel, “Surface damage growth mitigation on KDP/DKDP optics using single-crystal diamond micromachining,” in *Laser-Induced Damage in Optical Materials: 2003*, edited by G. J. Exarhos, A. H. Guenther, N. Kaiser, K. L. Lewis, M. J. Soileau, and C. J. Stolz, Vol. 5273, pp. 273–280, SPIE, Bellingham, WA, 2004.

# Laser-induced surface damage of optical materials: adsorption sources, initiation, growth, and mitigation

[7132-53]

## Questions and Answers

Q. What is the key parameter for your theoretical model which explains the different morphology difference for femtosecond damage and nanosecond damage? You know that in the femtosecond region the damage morphology is ablation and in the nanosecond regime, it is crack formation. What is the key parameter, which explains the transition from crack formation damage to ablation?

A. Well, I didn't talk about the femtosecond model, but it's been my understanding that in the femtosecond pulse you first deposit your energy in an electronic subsystem. By the time electrons start to transfer energy to the phonons, the pulse is gone. And, usually because deposition of the energy comes in such an extreme high power density, material usually goes through a phase explosion, so it's almost like a melting stage, but the material becomes overheated so it goes right away into the boiling. The Monte Carlo simulation using this finite element method of modeling very nicely shows this. In other words if you use this finite element approach of modeling this process, the ablation of material goes in an explosive manner. The heat is transferred rapidly to the surrounding matrix. If you are not generating much heat in the surrounding matrix, you are not generating such high temperatures. The key is, no high temperature, no high pressure, and hence no cracking.

A. Molecular dynamics simulation shows this very nicely. The conference on laser ablation discussed this in detail, showing how this happens, just passing the melting stage.